

Development and application of the Ascent-Drift-Descent Radiosonde System (ADDRS)

Xiaozhong Cao*¹, Qiyun Guo^{2,3,4}, Haowen Luo^{2,3,4}, Jincheng Wang⁵, Rongkang Yang^{2,3,4}, Die Xiao⁶, Yinfeng Liu⁷, Zhongliang Sun⁸, Shijun Liu⁹, Sijie Chen¹⁰, Anfan Huang^{2,3,4}, Guo Jianping¹¹, Peng Zhang*^{2,3,4}

¹ China Meteorological Administration, Beijing, China;

² Meteorological Observation Centre of China Meteorological Administration, Beijing, China;

³ State Key Laboratory of Environment Characteristics and Effects for Near-space, Beijing, China;

⁴ Engineering Technology Research Center for Meteorological Observation of CMA, Beijing, China;

⁵ CMA Earth System Modeling and Prediction Centre (CEMC), Beijing, China;

⁶ Hunan Key Laboratory of Near-space Meteorological Materials and Technology, Zhuzhou Research & Design Institute Co, Ltd, Zhuzhou, China;

⁷ Beijing Huayun Orient Detection Technology Co, Ltd., Beijing, China;

⁸ Allystar Technology (Shenzhen) Co.LTD. , Shenzhen, China;

⁹ Department of Advanced Technology Training of China Meteorological Administration, Beijing, China;

¹⁰ National Satellite Meteorological Centre of China Meteorological Administration, Beijing, China;

¹¹ Chinese Academy of Meteorological Sciences, Beijing, China;

Corresponding author: Xiaozhong Cao, caoxzh@cma.gov.cn, Peng zhang, zhangp@cma.gov.cn.

ABSTRACT. Balloon-borne radiosonde observations constitute a crucial component of meteorological sounding, which conducts a ground to upper-air “ascent phase” sounding. This paper introduces the Ascent-Drift-Descent Radiosonde System (ADDRS), an innovative system characterized by three observation phases—'Ascent-Drift-Descent' (ADD)—in which all three phases of sounding observation are executed through single balloon launch. Several key technologies were successfully developed, including the carrier (dual-mode balloon), the payload (System-on-Chip (SoC) module for radiosonde), Ground to upper-air data reception and control command transmission and data processing framework based on 'Internet cloud + Instrument terminal' was established. Data quality control methods and data assimilation techniques of ADDRS were also developed. An interactive experiment encompassing observations and forecasting was conducted to evaluate the quality of experimental data at each phase of ADDRS. Numerical assimilation and forecasting experiments showed a positive (albeit not yet statistically significant) impact on forecast quality for both general cases and for Tropical cyclone cases. The pre-operational launching and assimilation of more than 100 such radiosondes started on 1 July 2024 and provided data over one year, and the number of stations continues to grow.

1. Introduction

The upper-air meteorological sounding system (hereinafter referred to as 'sounding') constitutes a key element within comprehensive meteorological measurement framework (Ingleby et al., 2016a). It is responsible for gathering data on various meteorological elements such as temperature, humidity, pressure, wind speed, and wind direction from the surface up to heights of 30 km and beyond upper atmosphere (DuBois et al., 2002). This

37 system provides vertically observed meteorological data for weather forecasting, numerical weather prediction,
38 climate projection, scientific research, and the inspection and calibration of ground-based remote sensing
39 equipment (Seidel et al., 2009; Fujiwara et al., 2025). The integration of radiosonde technology with balloon-
40 borne soundings emerged in the 1930s, with early operational systems deployed in the 1940s; this technology
41 has since served as a primary tool for direct measurements of upper-air meteorological elements below 30 km
42 and is widely utilized on a global scale (Pettifer 2009; Gallice et al., 2011).

43 For nearly a century, these radiosondes have utilized the direct measurement method of “one balloon
44 launched, one profile”. The radiosonde ascends at a certain speed with the balloon expanding in volume due to
45 decreasing air pressure as altitude increases. Upon reaching a specific altitude, the balloon bursts, concluding
46 the measurement process. This methodology confines effective observations to the radiosonde's ascent phase
47 (Haig et al., 1958). The disposable nature of radiosondes and balloons necessitates significant costs for multiple
48 deployments. Consequently, economic constraints have led to reductions in sounding operations, such as
49 Russia's temporary reduction of launches from twice to once daily in 2015, impacting the forecasting accuracy
50 of numerical prediction models across Northern Hemisphere countries (Ingleby et al., 2016b).

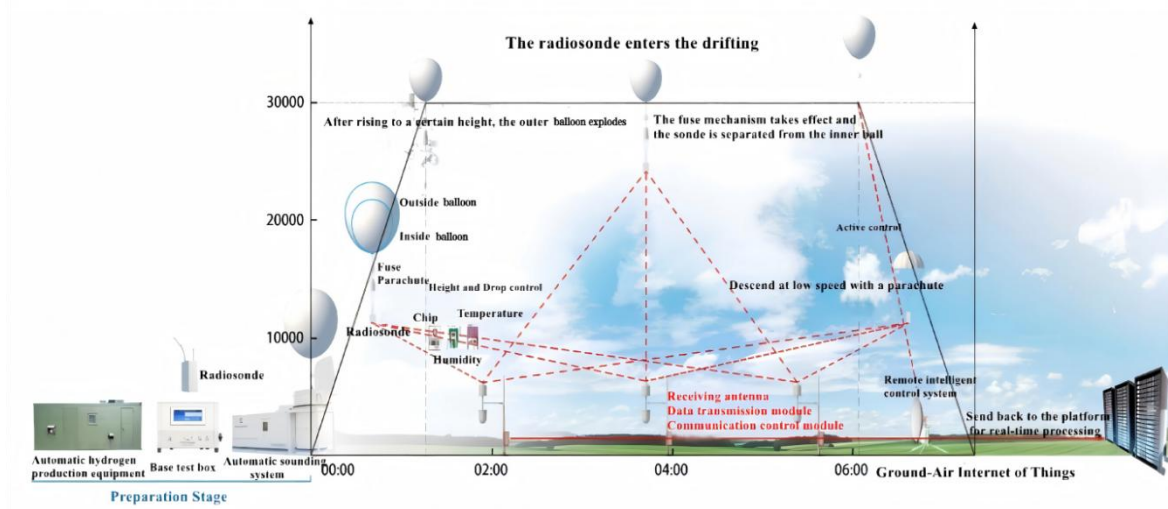
51 In recent decades, satellite soundings have played an increasing role in Numerical Weather Prediction
52 (NWP) and are now the observations contributing most to forecast skill (Bauer et al., 2015; Bormann et al.,
53 2019; WMO, 2024). While radio occultation data has gained importance as a reference standard (Bauer et al.,
54 2014), radiosonde profiles still provide an important contribution to forecast skill, help with the calibration and
55 validation of satellite soundings and allow independent verification of forecast fields. But the temporal
56 resolution of global radiosonde observations data remains limited, posing a significant challenge to its capacity
57 in fulfilling the requirements of routine forecasting. A notable concern arises from the scarcity of direct
58 measurement data during periods characterized by frequent severe convective activity, particularly in the hours
59 immediately following noon. Several studies have demonstrated that the frequent acquisition of descent
60 radiosonde data can enhance the accuracy of numerical weather forecasting. Some multi-year studies (Cohn et
61 al., 2013; Wang et al., 2015) suggest that assimilation of dropsonde data can reduce hurricane trajectory short-
62 range forecast errors by 10-15%. However other studies reviewed by Majumdar (2016) show less impact..

63 Additionally, several institutions are actively investigating techniques to obtain multiple radiosonde data
64 points from a solitary balloon launch. Illustrative projects include the multidisciplinary analysis of the African
65 monsoon and the measurement system research and forecasting experiments conducted in the Asia-Pacific
66 region, which utilize balloons to conduct drop soundings as they drift with stable upper-air winds over the
67 ocean (Raman et al., 2011; Johnson et al., 2024). Similarly, the Centre National d'Etudes Spatiales (CNES) of
68 the French Space Agency, has developed a Super Pressure Balloon (SPB) capable of floating in the stratosphere
69 for over three months (Roth et al., 2022). Additionally, the Tata Institute of Fundamental Research Balloon
70 Facility (TIFR-BF) in India has also contributed to this field by developing comparable systems (Anand et al.,
71 2021; Vernier et al., 2018; Vernier., 2022). Early stratospheric balloon systems encountered doubts concerning
72 their long-term feasibility for operational data collection, attributable to cost and ascent rate limitations (WMO-
73 No. 8., 2025). Additionally, slower ascent rates result in radiative errors issue. However, for wind vectors,
74 especially crucial upper-level winds, GPS-based positioning provides high-precision data less affected by the
75 ascent rate. The development of a new generation of commercial balloon systems has been changing this
76 landscape. Studies by Ratnam et al., 2014 and Ingleby et al., 2022 looked at the quality and value of radiosonde

77 descent data. This paper introduces a new sounding technology—the Ascent-Drift-Descent Radiosonde System
 78 (ADDRS). This system can improve the spatial and temporal frequency of soundings and provides an additional
 79 vertical profile as well as maintaining cost-effective, which acquires radiosonde measurement data throughout
 80 three phases—'Ascent-Drift-Descent' (ADD)—all with a single balloon launch (Cao et al., 2019; Cao et al.,
 81 2022).

82 **2. Synopsis of the Ascent-Drift-Descent Radiosonde System (ADDRS)**

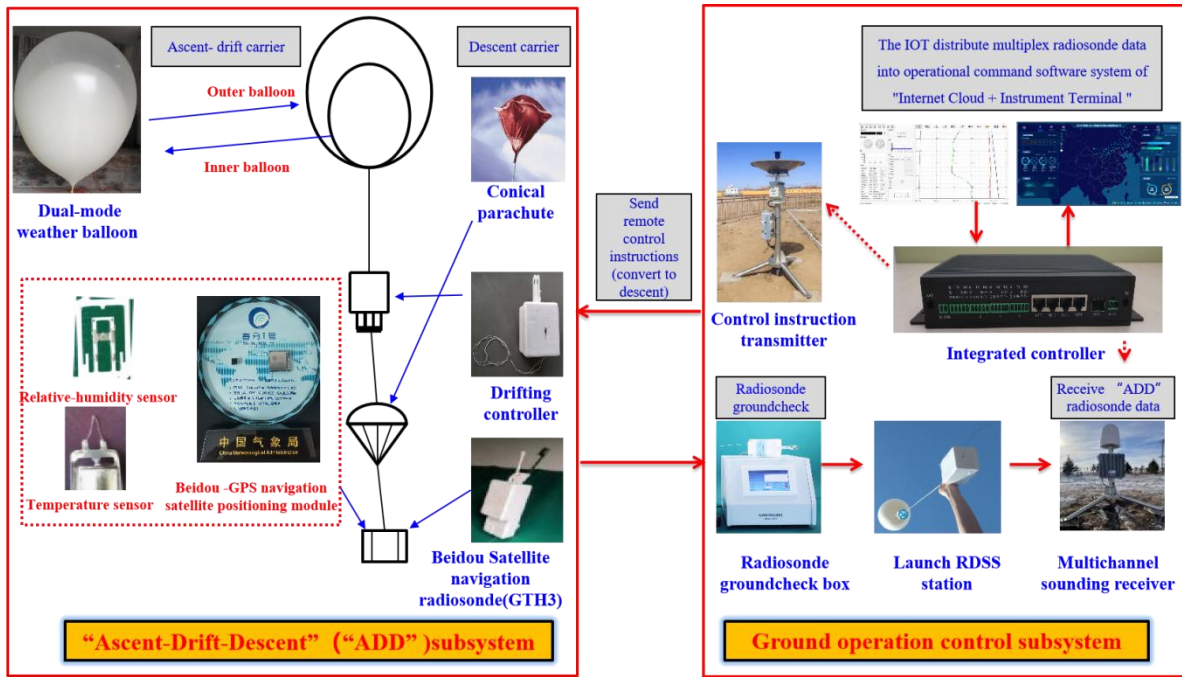
83 The ADDRS was developed by the Meteorological Observation Centre of the China Meteorological
 84 Administration (MOC of CMA) with other relevant organizations in China (hereinafter referred to as the
 85 'ADDRS research team'). It undertakes a three-phase upper-air measurement (Fig. 1).



86
 87 **Figure 1. Pre-operational principle diagram of the Ascent-Drift-Descent Radiosonde System (ADDRS).**

88 **Table 1. Main instruments and key functions of ADDRS.**

No	Subsystem	Instruments	Key Function
1	'ADD' subsystem	dual-mode balloon	'outer balloon' as ascent carrier, 'inner balloon' as drift carrier
2		parachute	parachute as the carrier of the descent phase
3		drifting controller	Adaptive control of drift and descent
4		radiosonde	The temperature, pressure, humidity, wind measurement meet the demand for long-term stratospheric observation
5	Ground operation control subsystem	Launch station	Manned radiosonde inspection, ground check, balloon inflation, and other balloon tasks
6		Multichannel sounding receiver	8 channels receive radiosonde data simultaneously
7		control command transmitter	In a weather-sensitive area without a station, the inner balloon can be detached and the descent started
8		operation management system	Real-time acquisition, transmission, quality control, and timely delivery of control instructions for ADDRS data, providing real-time high-quality data to weather analysis and numerical prediction models



89

90

Figure 2. Schematic representation of the equipment composition for ADDR.

91

92

93

94

95

96

97

98

99

100

101

102

103

104

105

106

107

108

109

110

111

112

113

114

The ADDR primarily consists of the 'ADD' subsystem and the ground operation control subsystem, as shown in Table 1 and Fig. 2. The 'ADD' subsystem encompasses a dual-mode balloon with a parachute, a drifting controller, and a radiosonde. The dual-mode balloon features a design where one balloon embedded within another, both made from a latex material similar to that of meteorological sounding balloons and filled with hydrogen. Upon inflation and launch of the dual-mode balloon, the 'ADD' subsystem at a rate of ascent between 5 and 7 m/s (WMO-No. 8., 2025). As it rises, the external air pressure decreases, causing the balloon to expand. At the predetermined altitude (generally between 28km and 30km), the outer balloon bursts due to its expanding volume, marking the conclusion of the ascent phase measurement. Given that the outer balloon bursts within the stratosphere, where vertical air movement is minimal, horizontal movement becomes predominant. The inner balloon does not burst, and the buoyancy of the inner balloon attains equilibrium with vertical stability, starting the drift phase.

After drifting for a predefined duration, which may vary from a couple of hours to over ten hours, the drifting controller separates the inner balloon from the rest of the ADDR equipment, thereby terminating the drift phase. The parachute is promptly deployed, facilitating the radiosonde in collecting data during the descent phase, while acting as its carrier. This descent persists until the equipment touches down, thereby completing the final phase of the 'ADD' process. At this point, ADDR has successfully completed the three-phase 'Ascent-Drift-Descent' measurement.

The ground operation control subsystem of ADDR comprises four main components in Table 1. The launch station operates with a high degree of automation for scheduled sequences, though the critical procedure for inflating the inner balloon to achieve drift requires operator supervision. Full automation of this process is under active development. Ground data-receiver can also be placed at the balloon launch station. However, its layout and function differ from the operational-ground data-receiver. Due to the ADDR drift phase, the horizontal distance between the descent point of the radiosonde and its launch point can exceed 500km, while radiosonde data reception has a maximum linear transmission distance of around 200km-300km.

115 Therefore, the traditional single-station, point-to-point radio communication mode of radiosondes is inadequate
116 for ADDRS data reception. Thus, the ground to upper-air communication system has been upgraded from point-
117 to-point to a multiple-to-multiple model. In areas through which the radiosonde's ADD phases may pass, ground
118 data-receivers are strategically deployed. This configuration enables multiple ground data-receivers to
119 concurrently receive data from a single radiosonde or alternatively, a single receiver to capture data signals from
120 several radiosondes simultaneously. Consequently, the ground data-receiver is designed as a P-band 8-channel
121 parallel data receiver, capable of receiving data from multiple radiosondes simultaneously. Additionally, control
122 command transmitters are located at the ground station and other locations. These transmitters send control
123 instructions from the ground to the drifting controller in the air through uplink communication. This system
124 allows for the adjustment of the drift phase elevation, termination of the drift phase, and switching to the descent
125 phase measurement as needed.

126 The operation management system acts as the brain of the entire ADDRS system. Multiple ground data-
127 receivers and control command transmitters are connected to the operation management system by the Internet.
128 These ground data-receivers continuously transmit data to the operation management system in real-time for
129 processing, display, and storage. Based on the ADDRS trajectory and specific weather and climate conditions,
130 comprehensive decision-making allows the operation management system to transmit control instructions to
131 control command transmitters which then relay them to the drifting controller in the air to execute the desired
132 functions.

133 The 'Internet cloud + Instruments terminal' architecture enables real-time, efficient, and bidirectional
134 communication across the entire network during the 'ADD' phases. This configuration supports the seamless
135 real-time acquisition, transmission, and quality control of ADDRS data while ensuring rapid data delivery for
136 weather forecasting. Consequently, it enhances the timeliness and availability of radiosonde data for forecasting
137 purposes.

138 **3. Critical scientific problems**

139 **3.1. Carrier technology**

140 **3.1.1 Study on the influence of atmospheric environment on the net lift power of balloons**

141 A multitude of meteorological factors, encompassing air temperature, air pressure, solar radiation, and
142 other external environmental conditions, coupled with the gas volume of the outer balloon directly influences
143 its net lift and burst altitude. Variations in pressure and temperature within the outer balloon, induced by
144 external meteorological conditions, interact with the expansion dynamics of the inner balloon. These factors, in
145 conjunction with the optimum volume of the inner balloon, collectively influence the altitude during the drift
146 phase and the static equilibrium of the inner balloon. Consequently, controlling the hydrogen inflation volume in
147 the dual-mode balloon presents a significant challenge.

148 The ADDRS research team conducted an in-depth theoretical analysis of the ascent and drift processes of
149 the dual-mode balloon, focusing on three areas: upper atmosphere model expansion, the balloon's dynamic
150 equation, and a thermodynamic model. This study led to the development of a coupling model that accounts for
151 the effects of atmospheric conditions on the balloon's net lift (from now on referred to as the 'coupling model')
152 (Liu, S. J et al., 2022). This model provides a theoretical foundation for determining the net lift force, ascent

153 velocity, and target burst altitude of the dual-mode balloon, enabling precise control of the mass of air in the
 154 balloons in the dual-mode balloon under varying meteorological conditions.

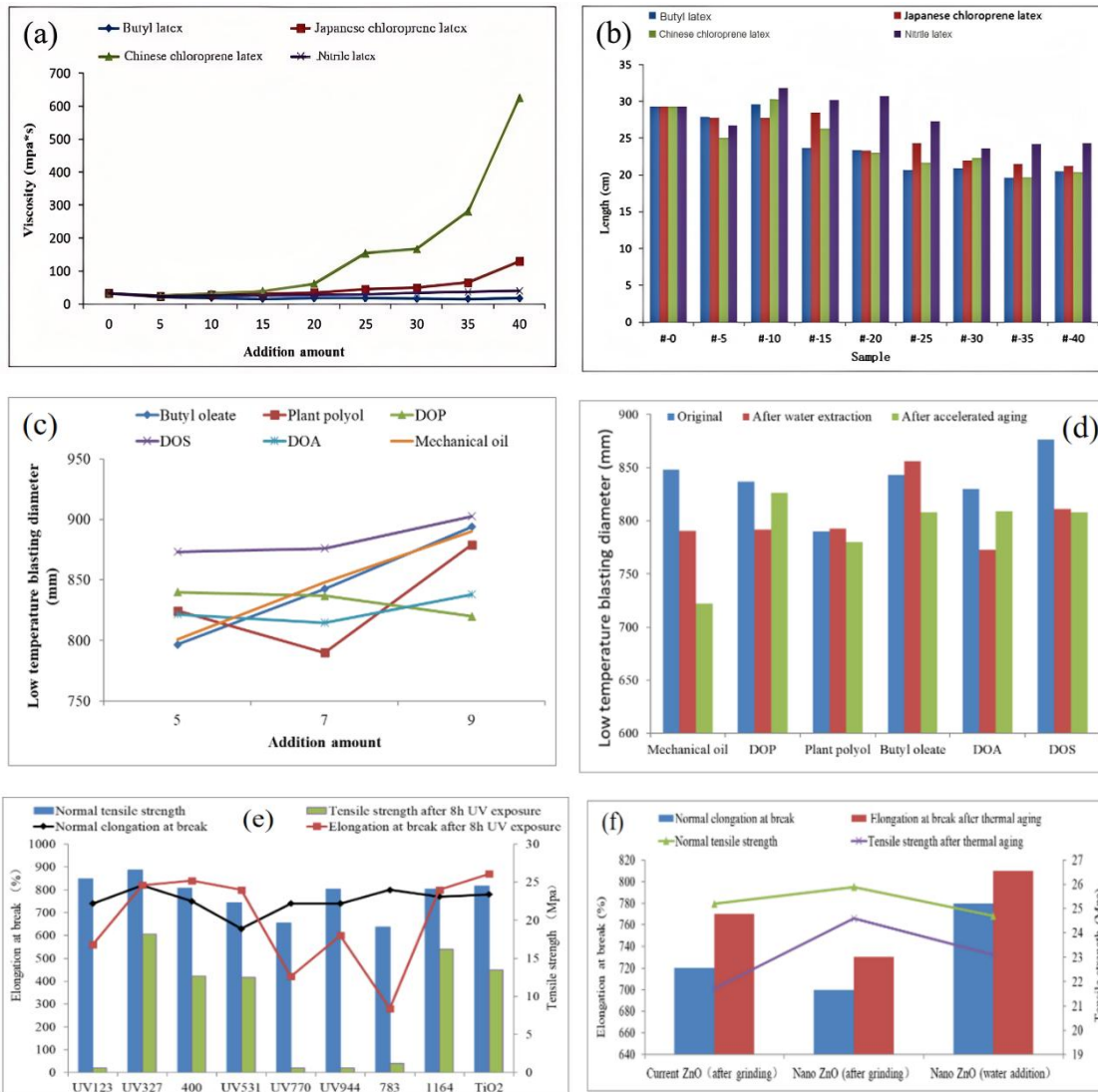
155 **Table 2. Inflate test results based on coupling model.**

Inflatable mode	Effective launch times	Drift number of times	Drift success rate	$\geq 4h$ number of times	$\geq 4h$ success rate
Algorithm software	611	479	78.40%	436	71.36%

156 Table 2 presents data from six stations (Changsha, Wuhan, Anqing, Yichang, Nanchang, and
 157 Ganzhou) situated along the middle and lower reaches of the Yangtze River in 2021. And based on the
 158 sounding balloon observation data in Guangdong from August 2022 to October 2023, the optimum volume
 159 capacities of related factors of the inner and outer balloons of the dual-mode sounding balloon on the success
 160 rate of the drift were studied, and a reasonable inflation scheme was established to improve the success rate of
 161 the drift. The research shows that the theoretical inflation amount of the inner balloon for drifting at the
 162 expected height is 55.6 mol. Affected by day and night conditions, the inflation amount during the day should be
 163 controlled at 52.6 ± 2 mol, and at night, it should be controlled at 57.6 ± 2 mol. The burst height of the outer
 164 balloon has a significant impact on the success rate of the drift. When the burst height of the outer balloon is
 165 within the expected height, the success rate of the drift can reach 82%. The success rate of the drift during the
 166 day is higher than that at night, and the success rate under clear sky conditions is higher than that under cloudy
 167 and rainy conditions. Under rainy conditions, the success rate of the drift is only 50.2%. After verification, the
 168 success rate of the drift can reach 93.5% by adopting the reasonable inflation scheme (Xu et al., 2025).

169 3.1.2 Performance improvement of the double - layer balloon

170 The ascent phase of meteorological sounding typically lasts between 1.5 and 2 hours. However, during the
 171 ADD process, the inner balloon of the dual-mode balloon is exposed to low temperatures, intense ultraviolet
 172 radiation, and high ozone concentrations for several hours or even up to ten hours. To address these challenges,
 173 the ADDRS research team conducted formulation tests to enhance the inner balloon resistance to these
 174 environmental factors, with a particular emphasis on natural latex modification, cold resistance, and anti-aging
 175 systems. Considering that latex hot air aging performance improves air tightness and balloons are exposed to
 176 prolonged sun exposure and hydrogen loss, the incorporation of a specific latex compound was found to
 177 augment durability. Fig. 3a and 3b show that the addition of latex formulas had minimal impact on the latex
 178 viscosity and the balloon appearance while improving its tensile strength and thermal aging resistance. Fig. 3c
 179 and 3d demonstrate that butyl oleate exhibits the lowest reduction in low-temperature burst performance after
 180 water extraction and accelerated aging, making it the best-performing cold-resistant agent. Consequently, this
 181 agent was integrated into the formula to bolster cold resistance. For the anti-aging system, illustrated in Fig.3e
 182 and 3f, nano zinc oxide, which can be diluted directly with water to replace traditional zinc oxide, was used.
 183 Additionally, we incorporated antioxidants to enhance the balloons' resistance against ultraviolet and ozone
 184 degradation. These formula improvements extend the inner balloon lifespan under harsh conditions of low
 185 temperature, intense UV radiation, and high ozone levels. This enhanced durability has been applied to the inner
 186 balloon, resulting in an extended service life and a high success rate during the drift phase (Zhu et al., 2021;
 187 Shen et al., 2020).



188

189

190

191 **Figure 3. Modification test of natural latex in the inner sphere:** (a) Four types of modified natural latex materials—
 192 Butyl latex, Japanese chloroprene latex, Chinese chloroprene latex, and Nitrile latex—were screened and added to
 193 natural latex using the homogenization method. (b) Physical properties of the modified natural latex pellet samples
 194 were evaluated for operation and thermal aging tensile testing. (c) Butyl oleate, Plant polyol, DiOctyl Phthalate (DOP),
 195 DiOctyl Sebacate (DOS), DiOctyl Adipate (DOA), and mechanical oil were added to natural latex as cold resistance
 196 agents. Cold resistance system test: The blasting diameters of six types of cold-resistant samples were tested using low-
 197 temperature blasting instruments at -85°C . (d) Low-temperature blasting diameters were measured for six types of
 198 raw, water-pumped, and aged samples with seven parts of cold-resistant agents added. Anti-aging system test: (e)
 199 Comparison of tensile properties among nine anti-aging agents—UV327, UV400, UV531, UV1164, and TiO₂ filler—
 200 with 0.2 parts of one-component anti-aging agent after eight hours of operation and ultraviolet aging. (f) Comparison
 201 of tensile properties after ozone aging between Nano ZnO and ZnO.

202 3.2 Payload technology

203 3.2.1 Performance improvement of the radiosonde

204 Due to ADDR S operates effectively across all three phases of the ADD process, requiring a minimum
 205 operation time of six hours. This extended operation necessitates a larger-capacity battery for the ADDR S
 206 radiosonde. Additionally, the radiosonde's weight affects the balloon's inflation volume, making it essential to
 207 reduce the radiosonde's weight where possible. Therefore, an integrated, lightweight, and low-power radiosonde
 208 is crucial, and the ADDR S research team developed a specialized SoC (System on Chip) module (named
 209 Equinox I) for CMA's GTH type of Beidou-based radiosonde.

210 The GTH3 employs a specialized SoC module of meteorological sounding and utilizes a multi-layer board
211 design and miniaturized components to reduce the size, weight, and power consumption. Compared to the
212 previous operational radiosonde (GTS12 radiosonde, WMO BUFR code:201), the GTH3 radiosonde (WMO
213 BUFR code:206) significantly reduce the overall size, weight, and power consumption of the device.
214 Furthermore, the amount of plastic and toxic materials in the circuit boards has also been substantially reduced
215 (Table 3).

216 The GTS12 and GTH3 radiosonde use the same PTU sensor, P(MEMS piezo-resistive), T(adopting self-
217 developed NTC bead thermistor (reduced from diameter $\leq 1\text{mm}$ to $\leq 0.4\text{mm}$) volume reduction, higher
218 sensitivity), U (capacitive thin-film polymer humidity sensor). The difference lies in that 'Instrumentation and
219 Methods' :

220 For P [Design the temperature compensation circuit and establish the correction equation by fitting the
221 sensor characteristic surface through multiple temperature segments and multiple pressure points to achieve
222 higher measurement accuracy.]

223 For T [Optimize the installation structure, included Angle and lead length through simulation analysis, and
224 effectively reduce the influence of solar radiation by improving the installation structure and coating process.]

225 For U [Optimize the Temperature compensation Correction Algorithm and humidity hysteresis Correction
226 Algorithm for Humidity sensors]

227 The GTH3 participated in WMO UAH2022 (Upper-Air Instrument Intercomparison Campaign organized
228 by the World Meteorological Organization (WMO) and co-organized by the Deutscher Wetterdienst (DWD) in
229 2022) with the results shown in Table 4. It is suitable for applications in ORUC (Operational and Research Use
230 in Climatology), including aeronautic meteorology, near/ultra-short-term forecasting, global numerical weather
231 prediction, and real-time monitoring (WMO IOM-143., 2024).

232 **Table 3. Comparison of parameters among RS41, GTH3 and GTS12 radiosonde.**

Radiosonde type	Positioning method	Volume (mm ³)	Weight (g)	Transmitting power (mW)	Working time (min)	Data Transmission Rate(bps)	Battery Weight (g)	Foam Packaging Weight (g)	Circuit boards Weight (g)
GTS12 radiosonde	Radar positioning	190×90×245	<400	400≤	>120	1200	<250	<70	<80
GTH3	Equinox I	155×65×60	<120(for one profile)	100≤	>240	Optional,2400,4800,9600	<40	<30	<50
		155×65×60	<170(for “ADD” three phase profile)	100≤	>640		<90	<30	<50
Vaisala RS41	u-blox G7020	155×60×46	109	60	>240	4800	76	/	/

233 **Table 4. The evaluation results of GTH3 radiosonde temperature, pressure, relative humidity, wind and geopotential height in WMO Instruments and Observation Methods Report**
 234 **No. 143. page.150(Note: The data are in the form of $\Lambda_{c,L} \delta_{c,L} \pm \epsilon_{c,L}$, where $\Lambda_{c,L}$ represents the individual measurement root mean square error, $\epsilon_{c,L}$ denotes the measurement**
 235 **uncertainty, $\delta_{c,L}$ is the measurement error, and $\sigma(\delta)$ indicates the measurement standard deviation. The planetary boundary layer (PBL) ranges from surface to 2 kilometers; the**
 236 **free troposphere (FT) ranges from 2 kilometers to the tropopause 12 kilometers are in the ; the upper troposphere/lower stratosphere (UTLS) ranges from 7 kilometers to 17**
 237 **kilometers; the middle and upper stratosphere (MUS) is above 17 kilometers up to the bursting point of the sounding balloon.)**
 238

Time	Height	Atmospheric temperature [K]	Relative humidity [%RH]	Geopotential height [m]	Pressure [hPa]	Wind (horizontal)direction[°]	Wind (horizontal)speed [m.s ⁻¹]	Wind (horizontal)vector [m.s ⁻¹]
Day	PBL	$0.18_{0.17}^{-0.05} \pm 0.03$	$7.00_{4.41}^{-5.43} \pm 0.74$	X	X	X	X	X
	FT	$0.12_{0.11}^{+0.05} \pm 0.04$	$8.75_{8.02}^{-3.50} \pm 0.60$	$5.9_{5.5}^{+2.0} \pm 1.8$	$0.4_{0.4}^{-0.0} \pm 0.1$	$3.6_{3.6}^{-0.4} \pm 0.2$	$0.2_{0.2}^{-0.0} \pm 0.0$	$0.3_{0.1}^{+0.2} \pm 0.0$
	UTLS	$0.09_{0.08}^{+0.01} \pm 0.03$	$7.73_{7.58}^{-1.55} \pm 0.40$	$13.2_{8.6}^{+10.0} \pm 3.8$	$0.4_{0.2}^{-0.3} \pm 0.1$	$2.5_{2.5}^{-0.2} \pm 0.3$	$0.2_{0.2}^{-0.0} \pm 0.0$	$0.3_{0.2}^{+0.2} \pm 0.0$
	MUS	$0.27_{0.16}^{-0.22} \pm 0.10$	$1.69_{0.82}^{+1.48} \pm 0.46$	$29.5_{17.9}^{+23.4} \pm 4.2$	$0.3_{0.1}^{-0.2} \pm 0.0$	$6.1_{6.1}^{-0.4} \pm 0.2$	$1.3_{1.3}^{-0.0} \pm 0.0$	$1.5_{1.5}^{+0.3} \pm 0.0$
Night	PBL	$0.38_{0.34}^{-0.18} \pm 0.05$	$4.72_{4.66}^{+0.74} \pm 0.15$	X	X	X	X	X
	FT	$0.15_{0.15}^{+0.02} \pm 0.02$	$6.41_{6.03}^{+2.16} \pm 0.11$	$5.8_{5.8}^{+0.4} \pm 0.4$	$0.5_{0.5}^{+0.1} \pm 0.2$	$2.6_{2.6}^{-0.2} \pm 0.2$	$0.2_{0.2}^{-0.0} \pm 0.0$	$0.2_{0.1}^{+0.2} \pm 0.0$
	UTLS	$0.12_{0.10}^{+0.06} \pm 0.05$	$6.82_{5.74}^{+3.70} \pm 0.26$	$11.5_{8.6}^{+7.7} \pm 3.4$	$0.3_{0.2}^{-0.1} \pm 0.1$	$2.4_{2.4}^{-0.1} \pm 0.1$	$0.2_{0.2}^{+0.0} \pm 0.0$	$0.2_{0.1}^{+0.2} \pm 0.0$
	MUS	$0.10_{0.10}^{-0.03} \pm 0.02$	$1.71_{0.74}^{+1.54} \pm 0.28$	$26.7_{16.8}^{+20.7} \pm 4.2$	$0.1_{0.1}^{-0.1} \pm 0.0$	$4.5_{4.4}^{-0.6} \pm 0.2$	$0.2_{0.2}^{-0.0} \pm 0.0$	$0.4_{0.3}^{+0.3} \pm 0.0$

240 **3.2.2 Drifting controller**

241 The drifting controller can be considered part of the ADDRS payload. It connects to an inner balloon above
242 and a parachute and radiosonde below. The controller fuses a wire with an instant high electric current,
243 triggering the mechanical device to disconnect the parachute and the radiosonde. The controller serves two main
244 functions during the drift phase:

- 245 1. Similar to the Windborne system, it is equipped with a ballast-dropping mechanism to control its weight,
246 allowing the inner balloon to better adapt to changes in altitude.
- 247 2. Separate the inner balloon from the other sounding equipment (parachute and radiosonde). Moreover, the
248 drifting controller can also initiate the fuse based on predetermined control rules, such as altitude limits
249 (≤ 18 km), specified time, the latitude and longitude of a designated area, or upon receiving commands
250 from the ground. This action can be taken before the drifting balloon is about to enter the specified area or
251 approach the maximum drift height. As a result, it will effectively end the drift phase, separating the
252 parachute and radiosonde from the balloon.

253 **3.3. Receiving radiosonde data and sending control instructions technology**

254 The ADDRS ground data-receiver utilizes a high-gain, low-power, ultra-compact omnidirectional antenna,
255 along with super-heterodyne architecture and multiple communication protocol algorithms, including time
256 division multiple access, frequency division multiple access, and code division multiple access (Gong et al.,
257 2021). It supports various frequency modulation modes and achieves a receiving sensitivity of better than -120
258 dBm (at 2400 bps), effectively addressing self-interference issues in multi-channel radiosonde data reception.
259 Additionally, the system incorporates narrow-band wireless communication technology to improve low-
260 elevation reception when the radiosonde drops below the receiving antenna's height, facilitating broad-area
261 coverage with a visual range radius for upper-air coverage of at least 200 km. The receiver can adapt to diverse
262 application scenarios, such as fixed stations, vehicles, and ships. With an average data reception rate of 99.7%,
263 the ground receiver at the Anqing station has demonstrated an impressive maximum reception distance of up to
264 487 km.

265 Unlike the one-way (downlink) communication mode used in radiosonde systems, the ADDRS control
266 command transmitter can send ground instructions to the drifting controller, with a linear communication range
267 extending beyond 300 km. This capability allows for precise control over the drifting controller to execute
268 actions such as releasing counterweights or separating the balloon from the parachute and radiosonde, enabling
269 the radiosonde to conduct drift phase measurements within the target area (Liu et al., 2021). During field tests,
270 over ten balloon discharge control commands were successfully transmitted, with the farthest reaching 403 km.

271 **3.4. 'ADD' measurement technology**

272 The details of the ADD measurement method are outlined by (Cao et al., 2019). The ascent phase
273 measurement technique adheres to the guidelines outlined in the CMA technical specification. The primary
274 research focus of the ADDRS is on the measurement techniques for the drift and descent phases.

275 **3.4.1 Temperature measurement method in the drift phase**

276 During the drift phase of ADDRS, the inner sphere of the dual-mode balloon moves with the horizontal
277 airflow in the stratosphere. The radiosonde's vertical movement, with the surrounding atmosphere, is minimal
278 and it can be approximately considered as drifting with the horizontal wind. The effect of radiation on the
279 temperature sensor during this phase is greater than during the ascent and descent phases, leading to
280 considerable measurement errors that are challenging to correct using general quality control algorithms.

281 Given the unique conditions of stratospheric air temperature measurement, the ADDRS research team
282 employs a multi-physical field, fluid-structure coupled computational fluid dynamics (CFD) approach to model
283 the behavior of the temperature sensor in high-altitude, low-wind-speed environments. This model calculates the
284 flow and the temperature field, accounting for radiation effects based on sun elevation, ventilation, sensor size,
285 and surface reflectivity. To ensure broad applicability, neural networks, and other mathematical methods are
286 used to fit the extensive simulation data, yielding practical error-correction equations (Yang et al., 2014).

287 Considering that there may be discrepancies between CFD simulations and real environmental conditions,
288 the ADDRS research team uses instruments such as low-pressure wind tunnels and solar simulators to create an
289 experimental platform. This setup simulates ventilation, air density, and solar radiation conditions during the
290 drift phase, allowing for the measurement of temperature errors due to solar radiation. These measurements
291 verify and refine the simulation-based error correction equations (Yang et al., 2022).

292 **3.4.2 Vertical wind data during the parachute descent**

293 Currently, due to the pendulum effect, vertical wind measurements cannot be performed in balloon-borne
294 soundings. The parachute-drop wind measurement model established by the WMO and NCAR does not address
295 vertical wind measurement directly (Wang et al., 2015), instead assuming a zero vertical wind speed. This
296 model assumes that the parachute-drop system is influenced only by gravity and vertical resistance, omitting
297 other factors like buoyancy, additional forces, and parachute rotation during descent. This limitation prevents
298 the analysis of vertical wind and also affects the accuracy of horizontal wind field calculations (Ingleby et al.,
299 2022).

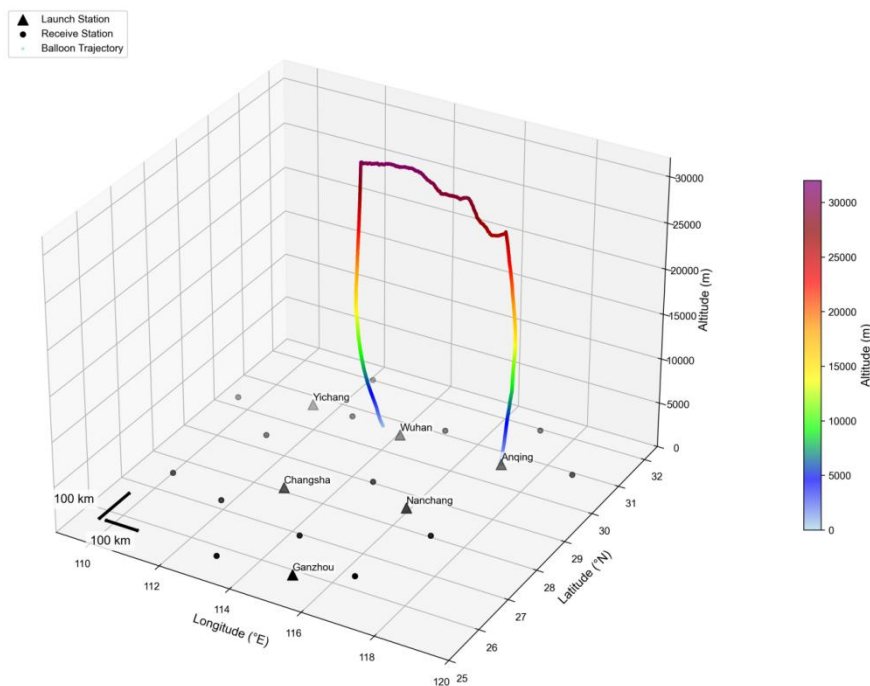
300 Therefore, the ADDRS research team developed a more comprehensive vertical wind measurement model
301 by considering all relevant forces acting on the balloon-launched and parachute descent dropsonde system,
302 utilizing the domestic Beidou-based radiosonde, shows significant promise. The Beidou-based radiosonde
303 demonstrated acceptable accuracy during both ascent and descent phases compared to the RS92 standard. The
304 key advantages identified were the ability to perform temporally intensive sounding observations (effectively
305 obtaining an 'ascent' and 'descent' profile from one launch) and the potential to spatially expand coverage
306 through the drift of the parachute, allowing for a 'one-station launch, multi-station reception' model. This
307 technology aligns with the trend towards automated, quantitative remote sensing in meteorological observation
308 (Guo et al., 2018). The string length between the balloon/parachute and the GTH3 radiosonde is standardized at
309 30 meters in manual launches. This length helps reduce sensor exposure to balloon wake effects but amplifies
310 pendulum motion in wind data. More than ten comparative tests were carried out for the selection of the conical
311 parachutes. The oscillation angle of conical parachute is less than 1° , which can ensure the rationality of the
312 Gaussian filtering correction filter window for the horizontal wind in the descent phase. Meanwhile, a larger
313 main parachute size can reduce the descent speed. Therefore, without considering the cost, a 'large conical
314 parachute' is recommended for the descent phase detection of ADDRS. And make sure the parachute area

315 should be tailored to match the radiosonde weight. The descent phase of ADDRS could achieve a low-level
 316 descent speed of $6 \text{ m/s} \pm 1 \text{ m/s}$ can be achieved in UTLS (upper troposphere and lower stratosphere (7-17km),
 317 and a swing angle below 5° , as well as a vertical wind measurement uncertainty of less than 1 m/s . These
 318 findings demonstrate that the model is effective for calculating vertical wind.

319 4. Field experiments and data quality verification

320 4.1. Field experiment in the middle and lower reaches of the Yangtze River Region

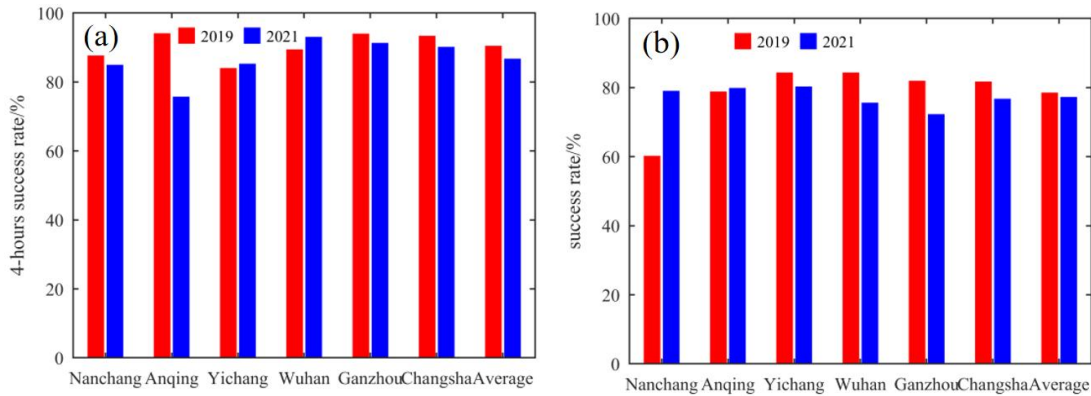
321 From 2019 to 2021, ADDRS conducted field tests and application research across a wide area in the middle
 322 and lower reaches of the Yangtze River in China. The research focused on measurement data processing
 323 methods, quality control algorithms, and application technologies across diverse scenarios. The ADDRS
 324 radiosondes were launched from six stations. They were Anqing, Wuhan, Yichang, Nanchang, Changsha, and
 325 Ganzhou, which located in Anhui, Hubei, Jiangxi, and Hunan provinces. A total of 14 ground radiosonde data
 326 receivers were strategically positioned around these six stations, spaced approximately 150 km apart. The test
 327 covered an area of 600,000 square kilometers, as shown in Fig. 4, and show a trajectory for ADDRS at the
 328 Anqing station at 12:00 UTC on 11 July 2021.



329 **Figure 4. The network distribution of ADDRS and an example of measurement: the trajectory for ADDRS at the**
 330 **Anqing station at 12:00 UTC on 11 July 2021. The black triangles represent balloon launch stations of ADDRS , while**
 331 **the black dots represent ADDRS receiving stations.**
 332

333 During the 13-month experimental period, 3,177 ADDRS launches were conducted, with 3,012 classified
 334 as effective launches, of which 2,369 achieved successful drifting. Among these, 2,136 launches resulted in
 335 drifting for more than 4 hours. The overall drifting success rate was 79%, with a 4-hour drifting success rate of
 336 71% (Fig. 5).

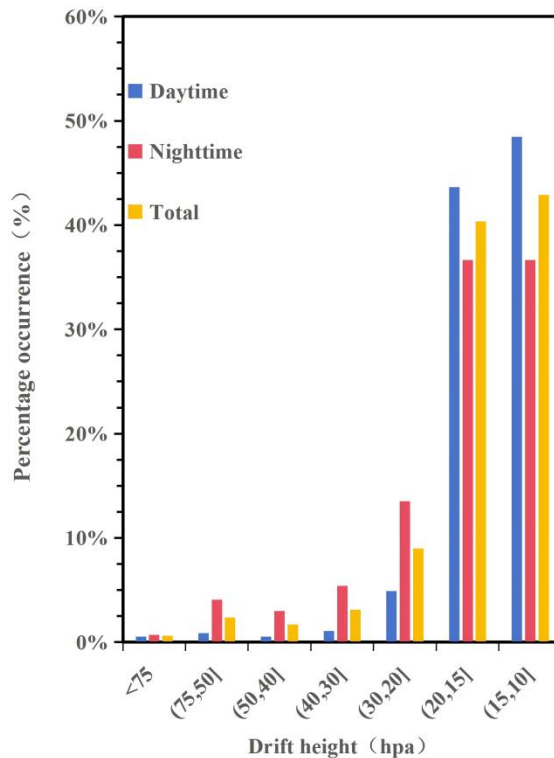
337



338

339 **Figure 5. The field experiment in the middle and lower reaches of the Yangtze River Region (2019-2021): (a) Drifting**
 340 **success rate; (b) 4-hour drifting success rate.**

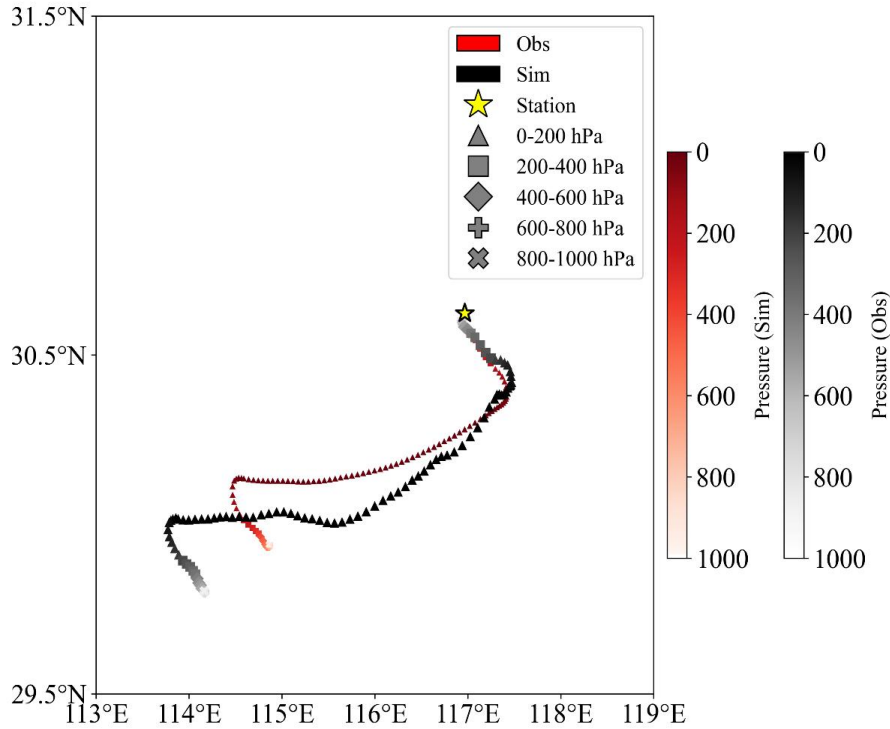
341 From March to September 2021, 2,427 'ADD' radiosonde launches were conducted, with 2,281 classified
 342 as effective launches, of which 1,772 achieved successful drifting. Among these, 1587 launches resulted in
 343 drifting for more than 4 hours. The overall drifting success rate was 78%, with a 4-hour drifting success rate of
 344 70%. The 1,772 successful drifts were analyzed (Fig. 6), and 937 were successful during the daytime,
 345 accounting for 53%. The successful nighttime drifting was 835 times, accounting for 47%, somewhat worse
 346 than the daytime performance. The drift heights ranging from < 75hPa (<18km) to 15hPa-10hPa (28km-32km)
 347 were statistically analyzed. The proportion of outer balloon explosion heights within 15hPa-10hPa (28km-32km)
 348 was the largest (43%). And the proportion of 20hPa-15hPa (26km-28km) is 40%, the proportion of 30hPa-
 349 20hPa (24km-26km) is 9%, and the total proportion of beyond 30hPa is 92%. Therefore, The drift height meets
 350 the GBON requirement of attaining at least 30hPa for a majority of ascents, with a subset of ascents also
 351 reaching the 10hPa level (WMO, 2020).



352

353 **Figure 6. The drifting height of sounding-forecasting interactive network experiment (2021) .**

354 Due to the limited availability of high frequency, continuous measurement data for the stratospheric
 355 atmosphere, experiments were conducted in the middle and lower reaches of the Yangtze River to obtain direct
 356 measurement data with high spatial and temporal density (Zhang et al., 2021). The simulated and observed
 357 trajectories are represented by red and black, respectively (Fig. 7). A color gradient based on pressure altitude is
 358 used to indicate the variation of trajectory height along the path.



359
 360 **Figure 7. Schematic diagram of the observed (black) and simulated (red) trajectories. The yellow pentagram**
 361 **indicates the radiosonde station. The color of each point represents the corresponding pressure level. Distinct**
 362 **markers are used every 200hPa to enhance visual differentiation.**

363 The balloons drifting of ADDRS radiosondes data in the above tropopause have been very useful for
 364 verification of FY-3D satellite temperature and humidity profiles (Zhou et al., 2023; Zhou et al., 2024). And
 365 application in observing certain features of gravity waves in the lower stratosphere (He et al., 2024; Yang et al.,
 366 2021) and feature extraction and analysis of atmospheric turbulence (Yang et al., 2023).

367 4.2 Data quality evaluation

368 Aiming at the characteristics of high-resolution ADDRS data for quantitative application, the ADDRS
 369 research team carefully evaluated ADDRS data using 31 data quality control methods based on the guidelines
 370 for CMA technical specification of operation upper-air meteorological observation (Wang, D et al. 2020). For
 371 the data quality of the ascent phase of the ADD radiosonde, refer to the results in Table 4. Additionally, the
 372 fifth generation of ECMWF (ERA5) global reanalysis (Hersbach et al., 2020) was used to evaluate the quality of
 373 four upper-air radiosonde observations stations' ADDRS data in Guangdong (Zhang, C.Z et al., 2025), and
 374 Table 5 demonstrates good consistency between the ascent and descent phases for temperature, u-wind, and v-
 375 wind (Yao et al., 2026). The conclusion is basically consistent with the results of Table 4 .

376 But for relative humidity (RH), different radiosonde manufacturers may adopt distinct saturation vapour
377 pressure (SVP) equations in calibrating humidity sensors. This difference in the choice of SVP equation can lead
378 to discrepancies in relative humidity measurements among different radiosonde types, especially under low-
379 temperature conditions. The ADDRS radiosonde humidity sensor is calibrated using the Goff (1957) SVP
380 equation recommended in earlier WMO publications (WMO, 2012). Moreover, relative humidity from the
381 ERA5 dataset is calculated using the Buck SVP equation. To ensure a more consistent comparison, relative
382 humidity was recalculated from temperature and specific humidity in the ERA5 dataset using the Goff (1957)
383 SVP equation, with the SVP assumed over liquid water only. The results show that the O–A bias and RMSE of
384 relative humidity under low-temperature conditions are reduced and become much more physically reasonable.

385 The wind data from the drift phase were validated through dedicated experiments involving accelerometers,
386 applying filtering principles consistent with Marlton et al. (2015). However, we note that the discrepancies in
387 the stratospheric drift phase (both wind and temperature) are larger. This is consistent with findings from other
388 studies comparing high-resolution radiosonde data with reanalyses (Pauley and Ingleby, 2022; Ingleby, 2017).
389 such differences are often attributed to representation errors arising from the inherent resolution mismatches.

390 A known warm bias, correlated with high initial descent rates (frequently >50 m/s), affects temperature
391 measurements during the early descent (Ingleby et al., 2022). Consistent with operational practice, data from the
392 initial high-descent-rate period in this study were filtered out prior to the comparison with reanalysis data
393 presented. This quality control step mitigates the impact of this bias on the statistical results.

394 **Table 5. Comparative analysis of after-quality control of ADDRS radiosonde data and ERA5 (O-A).**

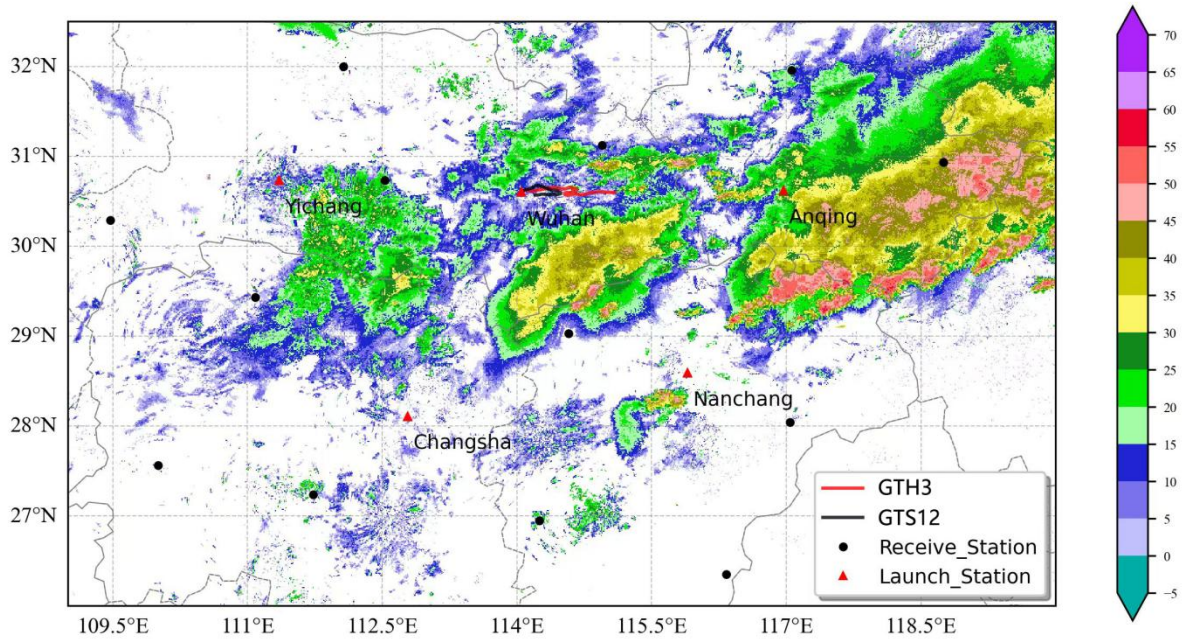
			U (m/s)		V (m/s)		T (K)		RH (% RH)	
			bias	std	bias	std	bias	std	bias	std
Ascent	Day	Above tropopause	0.03	1.73	0.11	1.91	-0.4	1.04	/	/
		Below tropopause	0.13	1.41	0.08	1.47	0.04	0.69	1.32	8.57
	Night	Above tropopause	-0.02	1.72	-0.01	1.87	0.01	1.02	/	/
		Below tropopause	0.13	1.4	0.02	1.46	0.08	0.66	1.62	8.32
Drift		Above tropopause	/	3.32	/	3.22	/	3.09	/	/
Descent	Day	Above tropopause	0.16	1.74	-0.02	1.9	0.9	1.14	/	/
		Below tropopause	0.14	1.65	0.01	1.7	0.42	0.75	-1.7	10.12
	Night	Above tropopause	0.16	1.73	0.03	1.84	0.21	1.06	/	/
		Below tropopause	0.15	1.67	0.05	1.67	0.04	0.73	0.5	10.47

395 5. Application of ADDRS in numerical forecasting techniques

396 5.1 A case study of weather analysis

397 Through long-term testing, the ADDRS have the potential to capture key information in convective system
398 monitoring. From July 8 to 9, 2021, a strong convective weather event with a long duration and a large impact
399 area occurred in the middle and lower reaches of the Yangtze River in China. Convection developed and moved
400 to northern Jiangxi, northern Zhejiang, southern Anhui, and southern Jiangsu overnight on July 8 (Fig.8). The
401 drifting trajectories of ADDRS radiosondes were from west to east, which aligned with the movement and

402 development direction of severe convection. The descent phase radiosondes of ADDRS provides effective
403 monitoring and insights in tracking the occurrence of the convective system and the changes in the ambient field.

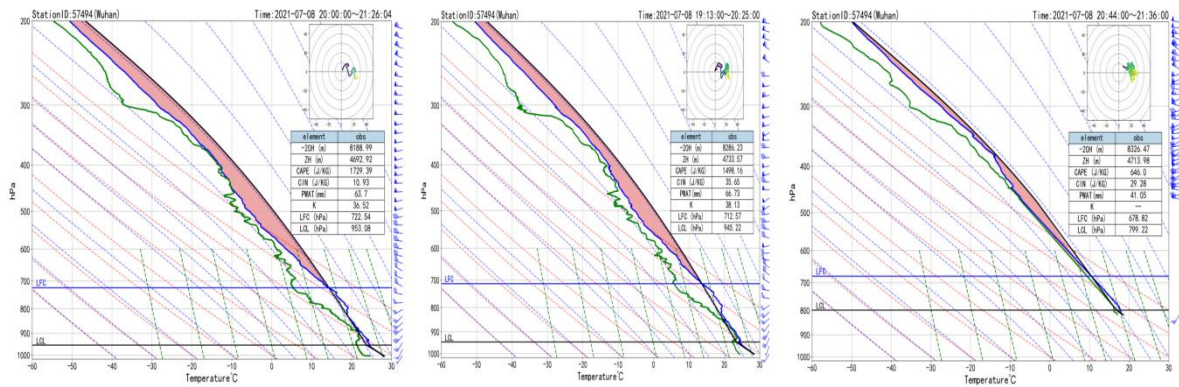


404

405 **Figure.8 The trajectory for GTH3 and GTS12 radiosonde at the Wuhan station and radar reflectivity image at 12:00**
406 **UTC on 8 July 2021.**

407 Figure 8 displays the trajectory data of the ADDRS and GTS12 radiosondes launched from the Wuhan
408 Meteorological Station. On the night of 8 November, at 11:15 UTC, Wuhan was situated on the western flank of
409 the main convective system. The ADDRS radiosonde was launched at this time from the station, followed by the
410 GTS12 radiosonde at 12:00 UTC from the same location. During the ascent phase, the curve of the ADDRS
411 radiosonde (Fig. 9b) exhibited a trend similar to that of the GTS12 (Fig. 9a). A comparison of the ascent-phase
412 data revealed that the convective available potential energy (CAPE) values differed between the two instruments
413 as convection developed. The GTS12 measured a CAPE of 1729.39 J/kg at 12:00 UTC, higher than the value of
414 1498.16 J/kg recorded by the ADDRS at 11:15 UTC.

415 Influenced by an upper-level westerly jet, the ADDRS sounding balloon drifted eastward toward the
416 Wuhan. At 13:30 UTC, ADDRS conducted descent phase measurements (Fig. 9c). As shown in the layer curve,
417 the CAPE value at 21:30 decreased compared with that at 12:00 UTC, dropping to 646.0J/kg, which was lower
418 than the energy recorded at the Wuhan station. There is still a westerly jet stream with wind speed greater than
419 20m/s beyond the upper-air of 500hPa level. The east of Wuhan proximity to the main body of convection, the
420 reduction in energy suggests intensive upward motion, leading to the reduction of effective potential energy and
421 further develop of convective. Notably, the GTS12 radiosonde, launched from Wuhan, ceased data collection
422 after the ascent phase, thus missing this crucial change. The descent phase of ADDRS demonstrates
423 robust monitoring capabilities and holds significant implications, as it can timely captures environmental
424 conditions favorable for convection onset and development, including wind patterns, effective potential energy,
425 and humidity at downstream locations. These findings enable researchers to analyze changes in the upper-air
426 field and the occurrence of catastrophic weather convective systems.



427

428 **Figure 9. Comparison of ADDRS and GTS12 radiosonde T-logP at the Wuhan station: (a) GTS12 radiosonde; (b)**
 429 **ascent phase of ADDRS radiosonde; (c) descent phase of ADDRS radiosonde.**

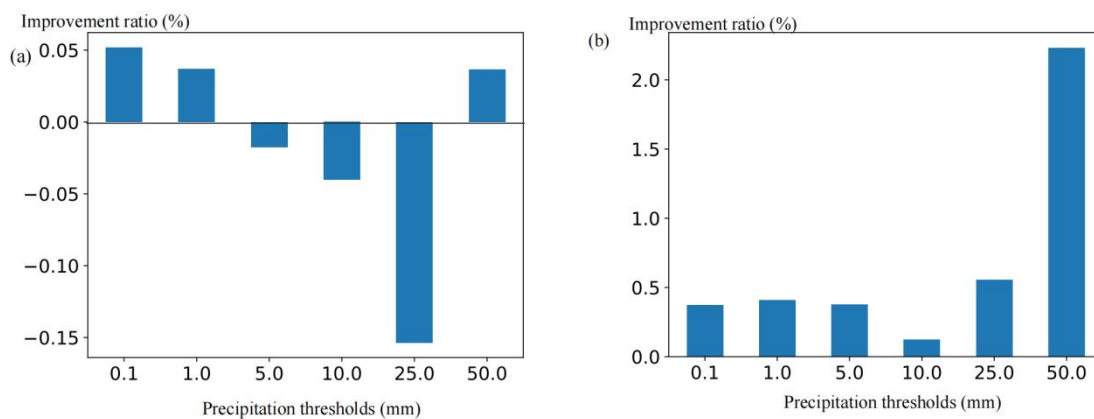
430 **5.2 Applications in numerical weather prediction (NWP)**

431 Unlike GTS12 radiosondes, the ADDRS radiosondes provide measurement data of both ascent and descent
 432 phase for numerical weather prediction (NWP), achieving a similar role to intensive sounding and providing
 433 more continuous, direct stratospheric measurement data (Zhang, X et al., 2025; Zhang, X.P et al. 2023). The
 434 Numerical Department of the China Meteorological Administration developed the key technology for ADDRS
 435 assimilation in the CMA-MESO 3DVar (three-dimensional variational mesoscale) (Zhuang et al. 2019) and
 436 CMA-GFS 4DVar systems (four-dimensional Variational Global Forecast System) (Wang, R. W et al., 2021).
 437 To avoid the tangent linear and adjoint models, the four-dimensional ensemble forecast error is introduced into
 438 the CMA global data assimilation system, and the Hybrid-4DVar assimilation scheme is developed. The
 439 batch cycling forecast experiments and typhoon forecast experiments are conducted and compared with the
 440 4DVar scheme (Gong et al., 2019; Wang, F et al., 2024). Specifically, this includes observation operators that
 441 consider drift positions and vertical spacing methods, such as selecting the nearest radiosonde data from the
 442 model layer for assimilation. But the assimilation of drift-phase observations faces three primary challenges:
 443 first, the large warm bias in daytime temperature measurements, which significantly impacts assimilation quality;
 444 second, the high likelihood of correlated observation errors due to the very high horizontal resolution of the data
 445 (~100 m along-track) compared to the model grid. Current operational systems do not account for these error
 446 correlations, necessitating data thinning to improve assimilation effectiveness. Third, determining the optimal
 447 data segmentation or "batching" strategy for the continuous trajectory. Treating the entire drift phase as a single,
 448 vertical profile at an average location introduces significant representativeness error, as it ignores the sonde's
 449 substantial horizontal displacement. We employed the CMA-MESO system to conduct a measurement data
 450 assimilation in the ADDRS descent phase across six test stations in the middle and lower reaches of the Yangtze
 451 River from July 1 to July 31, 2021. We set up the control test (CTL) as in the CMA-MESO system, and the
 452 observed data included traditional sounding data, ground reports, aircraft reports, cloud-guided wind, radar
 453 radial wind, GNSS occultation refractive index, and ground-based GNSS retrieval of the atmospheric whole-
 454 layer precipitation water. ADDRS data assimilation was added to the control CTL in the Down test.

455 The impact of the ADDRS descent phase measurement data on the precipitation forecast at CMA-MESO at
 456 03, 06, 09, 15, 18, and 21 UTC (termed the warm start times) was evaluated. Compared to the TS (Threat Score),
 457 the ETS (Equitable Threat Score) imposes stricter penalty for false alarms and missed reports, making the

458 scoring more equitable. The results of the one-month batch test indicate that assimilating ADDRS descent phase
 459 data improves precipitation forecasting skills, especially for heavy precipitation above a certain magnitude. Fig.
 460 10a and Fig. 10b illustrate the improvement rates in accumulated precipitation forecasting skills for the 0-12
 461 hour and 12-24 hour periods from the warm start time. Positive values indicate that the precipitation forecasting
 462 skills of the Down test are improved compared with those of the CTL test, while negative values indicate a
 463 decrease in forecasting skills for the Down test. The ETS scores for precipitation forecasts in the 0-12 hour
 464 range at thresholds of 0.1 mm, 1 mm, and 50 mm increased slightly, averaging about 0.04% (Fig. 10a). Due to
 465 the timeliness required for forecasting, the 12-24 hour precipitation forecast is of particular interest to
 466 forecasters. As illustrated in Fig. 10b, the Down test demonstrated enhanced ETS scores for precipitation
 467 forecasts across all levels within the 12-24 hour range, with an average increase of 0.7% at the 50 mm
 468 threshold and a notable 2.2% improvement specifically at this level. It is important to note that while these ETS
 469 improvements are consistent and positive, they have not yet reached conventional levels of statistical
 470 significance (e.g., $p < 0.05$) over the one-month test period, primarily due to the limited sample size of case
 471 studies. This underscores the preliminary yet promising nature of these findings.

472 In addition, we utilized CMA-MESO V5.1 to conduct Observing System Simulation Experiments (OSSE)
 473 under the ADDRS network nationwide. The results indicate that once the ADDRS network observation is
 474 implemented, the national precipitation forecast skills of the CMA-MESO fast cycle assimilation forecast
 475 system at warm startup time can improve by 2%-5%. The applications of ADDRS high-resolution data were
 476 quantitatively evaluated using a numerical model (Wang, R. W et al., 2023). After the application of ADDRS
 477 data in CMA-GFS 4DVar assimilation, the temperature analysis error at 06:00 and 18:00 was reduced by more
 478 than 2% and the average prediction skill of the CMA-MESO accumulated precipitation results for the 12-36
 479 hour period improved by 1% (Wang, J. C. et al., 2024).



480
 481 **Figure 10. Improvement rates of cumulative precipitation thresholds (mm) predictions for 0-12 hours (a) and 12-24**
 482 **hours (b) in the Down test compared to the control test.**

483 5.3 Applications in targeted observations

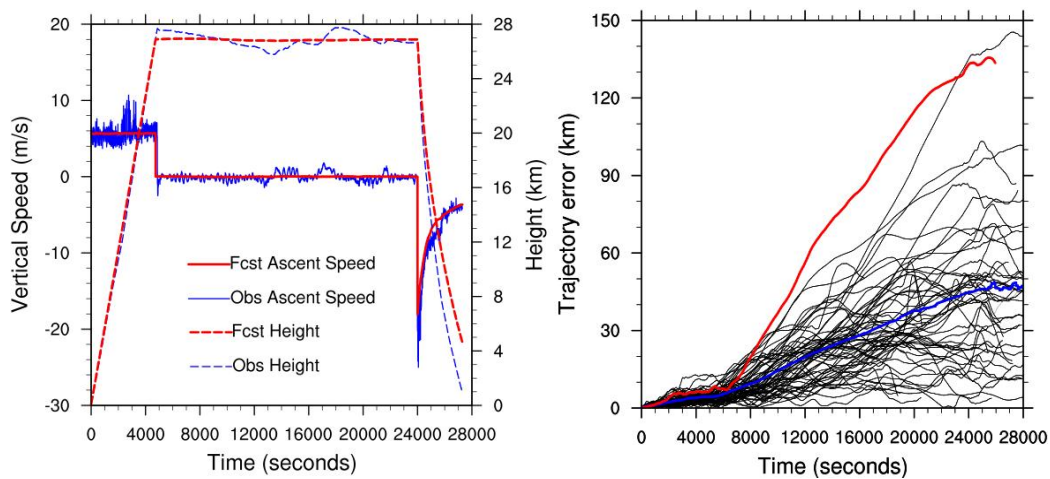
484 Targeted observations have sometimes been a frontier field in atmospheric science. They represent a
 485 possible method to address the shortcomings of conventional observation systems in monitoring extreme
 486 weather events. Furthermore, they sometimes enhance the initial field quality and forecast accuracy of
 487 numerical models (Majumdar, 2016). With its capacity for “ADD” measurement, the ADDRS has the potential

488 to conduct targeted observations in uninhabited areas, rarely observed regions, and during specific extreme
489 weather events. However, since the ADDRS lacks a steering system, accurate trajectory prediction is essential
490 for utilizing the descent phase for vertical measurements in these locations. This requires careful consideration
491 of appropriate drift height, launch time, and launch location, allowing the ADDRS sounding to be carried to the
492 target observation area by the ambient wind field.

493 In this context, a trajectory prediction and selection method based on high-resolution numerical weather
494 prediction technology has been proposed for ADDRS (Wang, J. C et al., 2021). Additionally, Majumdar (2016)
495 highlights that advancements in numerical weather prediction (NWP) systems—such as improved data
496 assimilation techniques and enhanced model resolution—have reduced the marginal contributions of individual
497 observing systems. Furthermore, the evaluation of targeted observations is constrained by factors including
498 flow-dependent conditions, limited sample sizes, and inconsistencies in verification metrics. Therefore, cost-
499 effective strategies for targeted observations necessitate exploration through multi-agency coordinated
500 observing system experiments, such as FSO studies (Magnusson et al., 2025).

501 5.3.1 Trajectory prediction method and software system

502 The issues of low temporal resolution and prediction accuracy associated with the linear extrapolation
503 method used in balloon trajectory prediction (Brown et al., 2024). The balloon trajectory equation is directly
504 embedded into a high-resolution numerical weather model system that utilizes a model atmospheric
505 environment with high temporal resolution (1-10 seconds) and high spatial resolution (1-3 km). This approach
506 enables precise simulation of vertical velocity during the ADDRS descent phase (Fig. 11a), enhancing the
507 accuracy of ADDRS trajectory prediction and the simulation of descent velocity. The average prediction error
508 for a 6-hour trajectory is less than 40 km (Fig. 11b).



509

510 **Figure 11. (a) Comparison of simulated (red line) and observed (blue line) vertical speeds of ADDRS radiosonde data**
511 **during the descent phase at the Anqing station at 11:17 on June 20, 2018; (b) Deviations of 63 pairs of simulated**
512 **ADDRS trajectories versus observed trajectories (black line), with the average deviation indicated by the blue line**
513 **and the largest forecast deviation shown by the red line.**

514 5.3.2 Trajectory selection method based on the collection idea

515 To observe the ADDRS in the target observation area, we proposed a method of elevation selection based
516 on ensemble forecasting, considering the characteristics of the atmospheric wind field as it varies with altitude.

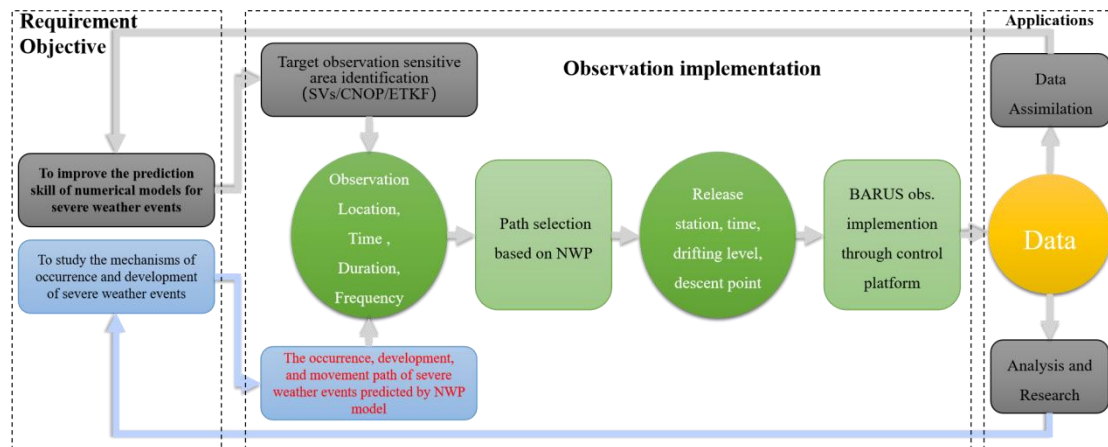
517 The main idea of this method is to predict the trajectories of all ADDRS stations at different drifting heights and
518 select the heights closest to the target observation area. The details are as follows:

- 519 1. Identify the positions and launch time: Given the positions $S_m(x_m, y_m, z_m)$ of M ADDRS launch stations and
520 the launch time t_r .
- 521 2. Select safe drift heights: Choose N safe drift heights h_1, h_2, \dots, h_n , that comply with civil aviation safety
522 regulations as flat drift heights.
- 523 3. Trajectory prediction: Utilize the trajectory prediction system to predict the ADDRS trajectories under the
524 above conditions within 12 hours, resulting in $T_{nm}(x, y, z, t)$ for N trajectories at each of the M launch
525 stations.
- 526 4. Calculate closest trajectory: From the $M \times N$ trajectories obtained in step 3, calculate the trajectory closest
527 to the target observation point. When the distance is less than the predetermined standard distance L_C that
528 can meet the requirements, the releasing ADDRS station and the drifting height H_s are selected, and the
529 time nearest to the target area is taken as the descent time t_s . If no suitable drift height meets the conditions,
530 the trajectory selection fails.
- 531 5. Implement target observation: Input the information regarding the ADDRS balloon launch station, drift
532 height, and descent time determined in step 4 into the ADDRS operation command system to execute the
533 target observation.

534 **5.3.3 Targeted observations experiment of Typhoon**

535 The ADDRS research team proposed a 'full chain' implementation for target observation using ADDRS
536 (Fig. 12). This implementation plan, designed to provide technical support for ADDRS applications in disaster
537 weather monitoring, forecasting, and mechanism research, encompasses three primary phases. Initially, the
538 requirements for target observation are established. These requirements fall into two categories: one focusing on
539 specific disaster weather events and the other on sensitive areas to improve future numerical prediction skills.
540 The target observation area is then determined based on the type of demand. For the first category, the specific
541 location of anticipated disaster weather is identified through numerical prediction results. For the second
542 category, the target observation location is determined using CMA-GFS singular vector technology.

543 Subsequently, the trajectory selection system is invoked to ascertain the ADDRS launch station, drift
544 height, launch and subsequent descent phases time, and other relevant information. This information is then
545 transmitted to the operation command system of ADDRS to guide the stations in implementing ADDRS
546 measurements. Ultimately, the ADDRS target observation data is distributed to users for application and
547 evaluation.



548

549

550

Figure 12. Technical route for targeted observations of typhoons and other severe weather using ADDRS and CMA-MESO models.

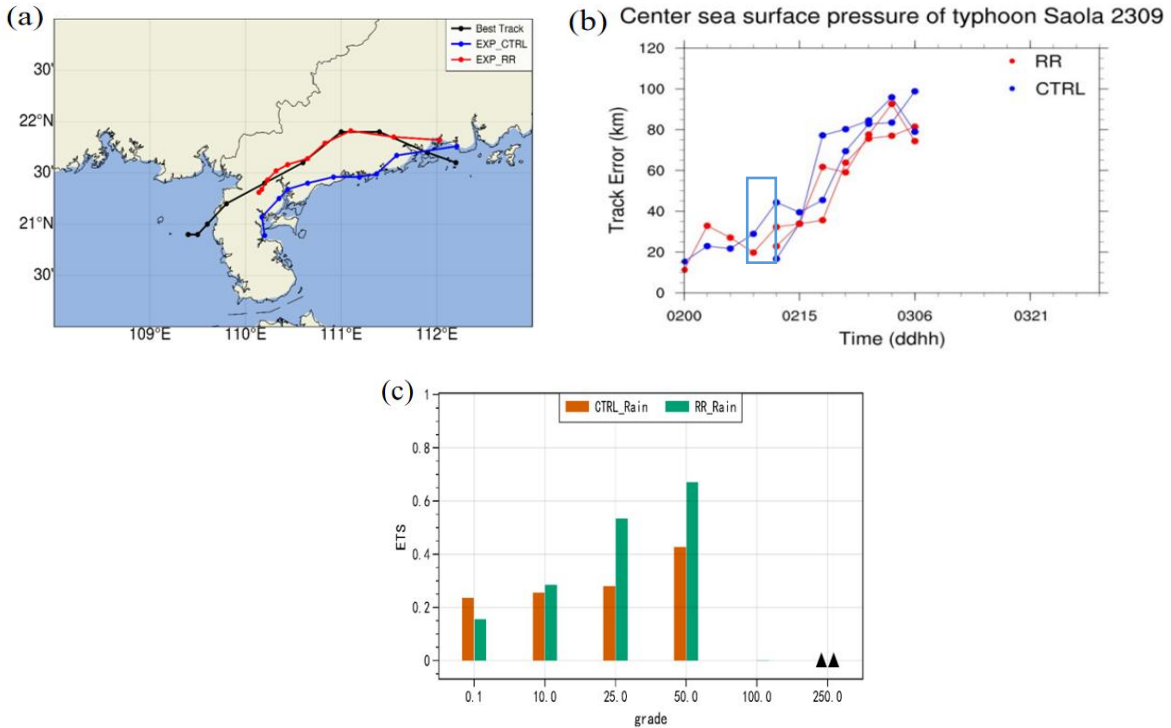
551

According to the implementation plan for ADDRS target observation (Zhang et al., 2021; Liu, L. H et al., 2022), we made a preliminary attempt to conduct a target observation experiment on Typhoon 2309 'SAOLA' (Lau et al., 2024) formed at 00 UTC on August 28, 2023. By 00 UTC on September 1, it was expected that 'SAOLA' would make landfall near Guangdong on September 2nd. Therefore forecasters sought profiles of the inner structure of Typhoon 'SAOLA'. Note also the importance of the steering flow and use of satellite data to analyse the wider environment of tropical storms (Magnusson et al, 2025). Using the typhoon trajectory predicted by CMA-GFS, we pinpointed the typhoon's position for 12:00 PM on September 2 post-landfall. The ADDRS trajectory selection system was then engaged to ascertain the balloon launch station and drift height that could reach or come closest to the typhoon area, ranging from the minimum navigation safety height of 21 km to 29 km. We set ten different drift levels at 1 km intervals, with trajectory predictions and simulations conducted from four radiosonde observations stations in Guangdong. Yangjiang radiosonde observations station in Guangdong was ultimately chosen for the launch, scheduled for 06:00 on September 2, 2023, with a drift level of 25 km.

564

We calculated the required hydrogen capacity for the dual-mode balloon, and the 'ADD' subsystem was prepared to be deployed by radiosonde observations station personnel. When the radiosonde reached the core area of 'SAOLA' the radiosonde dispatched commands to the 'SAOLA' controller via control command transmission equipment, successfully observing the descent phase 80 km from the center of Typhoon 'SAOLA'. The obtained ADDRS data was subsequently assimilated into the CMA_MESO 3DVar system. Test results indicated that after assimilating the data from the ADDRS descent phase, the forecast error for the typhoon trajectory reported since 06:00 on September 2, 2023, was reduced. Specifically, the typhoon trajectory error at 02:18 was reduced from 62.7 km to 35 km in the control test, marking an improvement of 44.18%. Additionally, precipitation forecasting techniques exhibited improvements: from 0.25 to 0.30 in the 10 mm scale, from 0.30 to 0.55 in the 25 mm scale, and from 0.45 to 0.70 in the 50 mm scale. These results effectively demonstrate the potential of ADDRS in target observation and numerical assimilation applications (Fig. 13). It is worth noting that the initial use of ADDRS for target observation served as a foundational attempt, paving the way for future ADDRS operations and maximizing its utility (Wen., et al., 2024).

576



577

578

579 **Figure 13. 2023-09-02 UTC 00-12h: (a) Control test (blue), ADDR data assimilation impact test (red), and optimal**
 580 **trajectory of Typhoon 'Saola' (black); (b) Comparison of sea level pressure at the central point of Typhoon 'Saola'**
 581 **between the control test (blue) and the ADDR data assimilation impact test (red); (c) ETS scores for 0-24 hours of**
 582 **precipitation forecast from control trials (orange) and ADDR data assimilation impact trials (green).**

583 6. Summary

584 ADDR represents a possible next-generation approach for upper air sounding, adding substantial
 585 flexibility compared to currently operational sounding systems, We developed a multi-station real-time
 586 reception system utilizing 'Internet cloud + Instruments terminal' technology. Additionally, uplink commands
 587 can be sent from the ground to facilitate descent measurements in designated areas and targeted observations in
 588 weather-sensitive regions. Following over five years of extensive research and numerous field tests, the
 589 instruments, software, and operation guidelines of the system have achieved a refined level of maturity. Starting
 590 January 1, 2024, ADDR already undergo operation experiments at four radiosonde observations stations in
 591 Guangdong, China. Since July 2024, a planned trial at 127 CMA radiosonde observation stations aims to
 592 achieve full operation capability by 2026. The positive impact of ADDR data assimilation demonstrated here,
 593 even if not yet statistically significant over a one-month sample, has shown considerable applicable promise.
 594 ADDR is a situational profiling technique that offers cost-effective upper-air measurements, making it suitable
 595 for widespread application in WMO's pre-operational sounding (e.g., RA II-18-I-DP-2). However, challenges
 596 remain, such as improving the drift success rate, enhancing relevant technologies, and fully leveraging the
 597 potential of continuous measurement data during the drift phase.

598

599 **Data Availability Statement:** The ADDR research team is currently building a new data-sharing platform
 600 (<https://www.r7tec.com/html/report/20040875-1.htm>), which will be available for scientific sharing to registered

601 users starting in December 2025. More data acquisition requires formal request to the corresponding author <
602 gqyaoc@cma.gov.cn> for restricted availability.

603 **Team list:** Xiaozhong Cao^{*1}, Qiyun Guo^{2,3,4}, Haowen Luo^{2,3,4}, Jincheng Wang⁵, Rongkang Yang^{2,3,4}, Die Xiao⁶,
604 Yinfeng Liu⁷, Zhongliang Sun⁸, Shijun Liu⁹, Sijie Chen¹⁰, Anfan Huang^{2,3,4}, Guo Jianping¹¹, Peng Zhang^{*2,3,4}

605 **Author contribution:** XC, PZ, conceptualization and methodology; QG and HL designed the experiments and
606 writing-original draft, supervision; JW, DX, JD, ZS, SL carried out the experiments; HL, QG, JW, RY, analyzed
607 the experimental results; HL, QG, GJ, SC, AH revised the paper and participated in the discussion. **Competing**
608 **interests:** The contact author has declared that none of the authors has any competing interests.

609 **Disclaime:** Copernicus Publications remains neutral with regard to jurisdictional claims made in the text,
610 published maps, institutional affiliations, or any other geographical representation in this paper. While
611 Copernicus Publications makes every effort to include appropriate place names, the final responsibility lies with
612 the authors.

613 **Acknowledgments:** The authors are thankful to the editor and all anonymous reviewers for their help in im-
614 proving this manuscript.

615 **Financial support:** This research has been supported by the National Natural Science Foundation of China
616 (grant no. U2442214); the National Key Research and Development Program (grant no. 2018YFC1506200); the
617 Innovation Team of the China Meteorological Administration (grant no. CMA2023QN11)

618

619 **References**

- 620 Anand, D., Kumar, B. S., and Ojha, D.: TIFR Zero-Pressure balloon program crosses a milestone, *Current*
621 *Science.*, 2021, 120, 1672-1678, <https://doi.org/10.18520/cs/v120/i11/1672-1678>, 2021.
- 622 Bauer, P., Thorpe, A., Brunet, G.: The quiet revolution of numerical weather prediction, *Nature.*, 2015, 525, 47–
623 55, <https://doi.org/10.1038/nature14956>, 2015.
- 624 Bauer, P., G. Radnóti., S. Healy., C. Cardinali.: GNSS Radio Occultation Constellation Observing System
625 Experiments, *Mon. Wea. Rev.* , 142, 555–572, <https://doi.org/10.1175/MWR-D-13-00130.1>, 2014.
- 626 Bormann, N., Lawrence, H., Farnan, J.: Global observing system experiments in the ECMWF assimilation
627 system, *ECMWF Technical Memorandum.*, 2019, 839, 24, <https://doi.org/10.21957/sr184iyz>, 2019.
- 628 Bauer, P., G. Radnóti., S. Healy., C. Cardinali.: GNSS Radio Occultation Constellation Observing System
629 Experiments, *Mon. Wea. Rev.*, 142, 555–572, <https://doi.org/10.1175/MWR-D-13-00130.1>, 2014.
- 630 Brown, D., Linz, M. & Leidich, J.: Seasonal and geographic viability of high altitude balloon navigation. *Sci*
631 *Rep.*, 14, 21861 (2024). <https://doi.org/10.1038/s41598-024-71445-9>, 2024.
- 632 Cao, X. Z., Xia, Y. C., Luo, H. W., Liu, L. H., Liu, Y. F., Liu, Z. Y., Li, X., Guo, R., and Guo, Q. Y.: Technical
633 development and prospect of meteorological sounding measurement, *J. Adv. Meteorol. Sci. Technol.*, 12,
634 27-36, <https://doi.org/10.3969/j.issn.2095-1973.2022.05.005>, 2022. (in Chinese)
- 635 Cao, X. Z., Guo, Q. Y., Yang, R. K.: Research of rising and falling twice sounding based on long-time interval
636 of flat-floating, *Chinese Journal of Scientific Instrument.*, 40(2): 198-204.
637 <http://yqyb.etmchina.com/yqyb/article/abstract/20190223?st=search>, 2019. (in Chinese)
- 638 Cohn, S., Hock, T., Cocquerez, P., & Cole, H.: Driftsondes: providing in situ long-duration dropsonde
639 observations over remote regions, *Amer. Meteor. Soc.*, 94, 1661–1674, [https://doi.org/10.1175/BAMS-D-](https://doi.org/10.1175/BAMS-D-12-00075.1)
640 12-00075.1, 2013.
- 641 DuBois, J. L., Multhaupt, R. P., and Ziegler, C. A.: Invention and Development of the Radiosonde with a Catalog
642 of Upper-Atmospheric Telemetering Probes in the National Museum of American History, *Smithsonian*
643 *Institution, Smithsonian Studies in History and Technology.*, 2002, 53, 1-78,
644 <https://doi.org/10.5479/si.00810258.53.1>, 2002.
- 645 Fujiwara, M., Sun, B., Reale, A., Cimini, D., Larosa, S., Borg, L., von Rohden, C., Sommer, M., Dirksen, R.,
646 Maturilli, M., Vömel, H., Kivi, R., Ingleby, B., Kramer, R. J., Demoz, B., Madonna, F., Carminati, F.,
647 Lewis, O., Candy, B., Thomas, C., Edwards, D., Noersomadi, Shimizu, K., and Thorne, P.: Justification for
648 high-ascent attainment for balloon radiosonde observations at GRUAN and other sites, *Atmos. Meas. Tech.*,
649 2025, 18, 2919–2955, <https://doi.org/10.5194/amt-18-2919-2025>, 2025.
- 650 Gallice, A., Wienhold, F. G., Hoyle, C. R., Immler, F., and Peter, T.: Modeling the ascent of sounding balloons:
651 derivation of the vertical air motion, *Atmos. Meas. Tech.*, 2011, 4, 2235-2253, [https://doi.org/10.5194/amt-](https://doi.org/10.5194/amt-4-2235-2011)
652 4-2235-2011, 2011.
- 653 Gong, N., Liu, Y. F., Ren, J., Wu, Q., and Hu, H. L.: A Novel Adaptive Resource Allocation Framework for
654 Sounding Networks, 2021 the 11th International Workshop on Computer Science and Engineering (WCSE
655 2021) ., 276-283, <https://doi.org/10.18178/wcse.2021.06.040>, 2021.
- 656 Gong, J. D., Liu, Y. Z., Zhang, L.: A study of simplification and linearization of the NSAS deep convection
657 cumulus parameterization scheme for 4D-Var, *Acta Meteorologica Sinica.*, 77, 595-616,
658 <https://doi.org/10.11676/qxxb2019.048>, 2019. (in Chinese)

659 Guo, Q. Y., Yang, J. C., Yang, R. K., Qian, Y., and Cao, X. Z.: Evaluation of wind performance of domestic
660 Beidou dropsonde of ball-loading, *J. Nanjing Univ. Inf. Eng.: Nat. Sci. Ed.*, 10,
661 12, <https://doi.org/10.13878/j.cnki.jnuist.2018.05.014>, 2018. (in Chinese)

662 Haig, T. O., and V. E. Lally.: Meteorological Sounding Systems, *Bull. Amer. Meteor. Soc.*, 39, 401–
663 409, <https://doi.org/10.1175/1520-0477-39.8.401>, 1958.

664 He, Y., Zhu, X., Sheng, Z., and He, M.: Identification of stratospheric disturbance information in China based
665 on the round-trip intelligent sounding system, *Atmos. Chem. Phys.*, 2024, 24, 3839–3856,
666 <https://doi.org/10.5194/acp-24-3839-2024>, 2024.

667 Hersbach, H., Bell, B., Berrisford, P., Hirahara, S., Horányi, A., Muñoz - Sabater, J., Nicolas, J., Peubey, C.,
668 Radu, R., Schepers, D., Simmons, A., Soci, C., Abdalla, S., Abellan, X., Balsamo, G., Bechtold, P., Biavati,
669 G., Bidlot, J., Bonavita, M., De Chiara, G., Dahlgren, P., Dee, D., Diamantakis, M., Dragani, R., Flemming,
670 J., Forbes, R., Fuentes, M., Geer, A., Haimberger, L., Healy, S., Hogan, R. J., Hólm, É., Janisková, M.,
671 Keeley, S., Laloyaux, P., Lopez, P., Lupu, C., Radnoti, G., de Rosnay, P., Rozum, I., Vamborg, F.,
672 Villaume, S., Thépaut, J. - N.: The ERA5 global reanalysis, *Q. J. R. Meteorolog.*
673 *Soc.*, <https://doi.org/10.1002/qj.3803>, 2020.

674 Ingleby, B., Pauley, P., Kats, A., Ator, J., and Weedon, R.: Progress toward high-resolution, real-time
675 radiosonde reports, *Bull. Amer. Meteor. Soc.*, 97, 2149–2161, [https://doi.org/10.1175/BAMS-D-15-](https://doi.org/10.1175/BAMS-D-15-00169.1)
676 00169.1, 2016a.

677 Ingleby, B., Rodwell, M., Isaksen, L.: Global radiosonde network under pressure, *ECMWF Newsletter No. 149*
678 – Autumn 2016., pp. 25 - 30, [https://www.ecmwf.int/sites/default/files/elibrary/2016/18147-global-](https://www.ecmwf.int/sites/default/files/elibrary/2016/18147-global-radiosonde-network-under-pressure.pdf)
679 radiosonde - network - under - pressure.pdf, 2016b.

680 Ingleby, B.: An assessment of different radiosonde types 2015/2016. *ECMWF Technical Memorandum No. 807*,
681 69 pp, <https://doi.org/10.21957/0nje0wpsa>, 2017.

682 Ingleby, B., Motl, M., Marlton, G., Edwards, D., Sommer, M., von Rohden, C., Vömel, H., and Jauhiainen, H.:
683 On the quality of RS41 radiosonde descent data, *Atmos. Meas. Tech.*, 2022, 15, 165-
684 183, <https://doi.org/10.5194/amt-15-165-2022>, 2022.

685 Johnson, A., Wang, X., Hutchinson, T., and Creus-Costa, J.: Impact of WindBorne observation assimilation on
686 prediction of a TPV merger case from THINICE, *J. Geophys. Res. Atmospheres.*, 129,
687 e2024JD041395, <https://doi.org/10.1029/2024JD041395>, 2024.

688 Lau, D.S., Chan, W.S., Wong, Y.C., Lam, C.C., Chan, P.W.: Hindcast Insights from Storm Surge Forecasting of
689 Super Typhoon Saola (2309) in Hong Kong with the Sea, Lake and Overland Surges from Hurricanes
690 Model, *Atmos.*, 15, 17, <https://doi.org/10.3390/atmos15010017>, 2024.

691 Liu, S. J., Yang, R. K., Cao, X. Z., Guo, Q. Y., Cheng, K. Q., Kan, Z. P., and Wang, J. C.: Analysis and
692 Numerical Experiment of the Horizontal Drift Round-trip Sounding Balloon's Dynamic and Thermal
693 Process in the Adjacent Space, *Chin. J. Atmos. Sci.*, 46, 788–804, [https://doi.org/10.3878/j.issn.1006-](https://doi.org/10.3878/j.issn.1006-9895.2110.20252)
694 9895.2110.20252, 2022. (in Chinese)

695 Liu, Y. F., Zhou, Y. Y., Du, J. P., Liu, D., Ren, J., Chen, Y. H., Zhang, F., and Chen, J. P.: RTP-GRU:
696 Radiosonde Trajectory Prediction Model Based on GRU, in *Proceedings.*, 24, [https://doi.org/10.1007/978-](https://doi.org/10.1007/978-981-15-8462-6_61)
697 981-15-8462-6_61, 2021.

698 Liu, L. H.; Han, Y.; Xia, Y. C.; Guo, Q. Y.; Gao, W.; Guo, J. P.: Investigation of Atmospheric Dynamic and
699 Thermodynamic Structures of Typhoon Sinlaku (2020) from High-Resolution Dropsonde and Two-Way
700 Rawinsonde Measurements, *Remote Sens.*, 14, 2704. <https://doi.org/10.3390/rs14112704>, 2022.

701 Magnusson, L., Majumdar, S.J., Dahoui, M.L., Bormann, N., Bonavita, M., Browne, P.A., Brown, A.R., De
702 Chiara, G., Duncan, D.I., English, S., Geer, A.J., Healy, S., Ingleby, B., McNally, A.P., Pappenberger, F.,
703 Prates, F., Rabier, F., de Rosnay, P., Rennie, M.P., Warrick, F.: The role of observations in ECMWF
704 tropical cyclone initialisation and forecasting, *Q. J. R. Meteorolog. Soc.*, 151(768),
705 e4924, <https://doi.org/10.1002/qj.4924>, 2025.

706 Majumdar, S.J.: A review of targeted observations, *Bull. Am. Meteorol. Soc.*, 97, 2287-
707 2303, <https://doi.org/10.1175/BAMS-D-14-00259.1>, 2016.

708 Marlton GJ, Harrison RG, Nicoll KA, Williams PD.: A balloon-borne accelerometer technique for measuring
709 atmospheric turbulence, *Rev. Sci. Instrum.*, 86, 016109, <https://doi.org/10.1063/1.4905529>, 2015.

710 Pauley, P.M., and Ingleby, B.: Assimilation of in-situ observations, In S.K. Park & L. Xu (Eds.), *Data*
711 *Assimilation for Atmospheric, Oceanic and Hydrologic Applications (Vol. IV)*(pp. 293–371). Springer,
712 Cham, https://doi.org/10.1007/978-3-030-77722-7_12, 2022.

713 Pettifer, R. E.: From Observations to Forecasts - Part 2. The development of in situ upper air measurements,
714 *Weather*, 2009, 64, <https://doi.org/10.1002/wea.484>.

715 Raman, M. R., Ratnam, M. V., Rajeevan, M., Rao, V. V. M. J., Rao, S. V. B.: Intriguing Aspects of the
716 Monsoon Low-Level Jet over Peninsular India Revealed by High-Resolution GPS Radiosonde
717 measurements, *J. Atmos. Sci.*, 68, 1413–1423, <https://doi.org/10.1175/2011JAS3611.1>, 2011.

718 Ratnam, M. V., Pravalika, N., Babu, S. R., Basha, G., Pramitha, M., Murthy, B. V. K.: Assessment of GPS
719 radiosonde descent data, *Atmos. Meas. Tech.*, 7(4), <https://doi.org/10.5194/amt-7-1011-2014>, 2014.

720 Roth, S., and Yoder, C. D.: Balloon missions soar to new heights, *Aerospace America.*, 60(11), 35-35.
721 <https://aerospaceamerica.aiaa.org/year-in-review/balloon-missions-soar-to-new-heights>, 2022.

722 Seidel, D. J., Berger, F. H., Diamond, H. J., Dykema, J., Goodrich, D., Immler, F., Murray, W., Peterson, T.,
723 Sisterson, D., Sommer, M., Thorne, P., Vomel, H., & Wang, J.: Reference Upper-Air Observations for
724 Climate: Rationale, Progress, and Plans, *Bulletin of the American Meteorological Society.*, 90(3), 361-
725 369, <https://doi.org/10.1175/2008BAMS2540.1>, 2009.

726 Shen, Z. P., Pan, X. Z., and Yi, Y. L.: Preparation and properties of modified nano-clay/natural latex composites,
727 *J. Rubber Ind.*, 67, 4, <https://doi.org/10.12136/j.issn.1000-890X.2020.08.0580>, (in Chinese)

728 Vernier, J. - P., Fairlie, T. D., Deshler, T., Ratnam, M. V., Gadhavi, H., Kumar, B. S., Natarajan, M., Pandit, A.
729 K., Raj, S. T. A., Kumar, A. H., Jayaraman, A., Singh, A. K., Rastogi, N., Sinha, P. R., Kumar, S., Tiwari,
730 S., Wegner, T., Baker, N., Vignelles, D., Stenichikov, G., Shevchenko, I., Smith, J., Bedka, K., Kesarkar, A.,
731 Singh, V., Bhate, J., Ravikiran, V., Rao, M. D., Ravindrababu, S., Patel, A., Vernier, H., Wienhold, F. G.,
732 Liu, H., Knepp, T. N., Thomason, L., Crawford, J., Ziemba, L., Moore, J., Crumeeyrolle, S., Williamson,
733 M., Berthet, G., Jégou, F., Renard, J. B.: Batal: The Balloon Measurement Campaigns of the Asian
734 Tropopause Aerosol Layer, *Bull. Am. Meteorol. Soc.*, 99, 955–973, <https://doi.org/10.1175/BAMS-D-17-0014.1>, 2018.

736 Vernier, H., Rastogi, N., Liu, H., Pandit, A. K., Bedka, K., Patel, A., Ratnam, M. V., Kumar, B. S., Zhang, B.,
737 Gadhavi, H., Wienhold, F., Berthet, G., and Vernier, J.-P.: Exploring the inorganic composition of the

738 Asian Tropopause Aerosol Layer using medium-duration balloon flights, *Atmos. Chem. Phys.*, 22, 12675–
739 12694, <https://doi.org/10.5194/acp-22-12675-2022>, 2022.

740 Wang, D., Wang, J. C., Tian, W. H., Guo, Q. Y.: Quality control and uncertainty analysis of Round - trip
741 drifting sounding system data, *Chinese J. Atmos. Sci.*, 44, 20, [https://doi.org/10.3878/j.issn.1006 -](https://doi.org/10.3878/j.issn.1006-9895.1912.19203)
742 9895.1912.19203, 2020. (in Chinese)

743 Wang, R. W., Han, W., Tian, W. H., Gong, J. D.: Blacklist Design of AMDAR Temperature Data and Their
744 Application in the CMA-GFS, *J. Trop. Meteorol.*, 27, 368–377, [https://doi.org/10.46267/j.1006-](https://doi.org/10.46267/j.1006-8775.2021.032)
745 8775.2021.032, 2021.

746 Wang, F., Gong, J. D., Wang, R. C., Chen, Y. D.: A methodological study of the CMA global hybrid four-
747 dimensional variational data assimilation system, *Acta Meteorol. Sin.*, 82(5), 709–
748 720, <https://qxxb.cmsjournal.net/cn/article/doi/10.11676/qxxb2024.20230140>, 2024. (in Chinese)

749 Wang, R. W., Wang, J. C., Wang, D., Tao, Y. W., Tian, W. H.: Study on the Influence of Return Sounding
750 Observation System Based on CMA-MESO, *Meteorol. Mon.*, 49(1), 52–
751 61, <https://doi.org/10.7519/j.issn.1000-0526.2022.032601>, 2023. (in Chinese)

752 Wang, J. C., Wang, D., Wang, R. W., Tan, J., Rong, N.: Assimilation of Round-Trip Horizontal Drift
753 Radiosonde Data in CMA-MESO 3DVar and Its Impact on Model Forecast, *Meteorol. Mon.*, 50(2), 50–
754 60, <https://doi.org/10.7519/j.issn.1000-0526.2023.110501>, 2024. (in Chinese)

755 Wang, J. C., Wang, D., Yang, R. K., Cao, X. Z., Guo, Q. Y.: A Return Radiosonde Trajectory Forecast Method
756 and Its Preliminary Evaluation Based on High Resolution Numerical Weather Prediction Model, *Chinese J.*
757 *Atmos. Sci.*, 45, 651–663, [https://doi.org/10.3878/j.issn.1006 - 9895.2012.20186](https://doi.org/10.3878/j.issn.1006-9895.2012.20186), 2021.

758 Wen, Q. S., Zhang, X. F., Hu, S., Zhao, P. T., Zhong, S. X., Liu, Z. Y., Zhao, Z. K., Liang, J. H., Dai, G. F.,
759 Zhang, C. Z., Li, M. J., Huang, L.: Collaborative assimilation experiment of Beidou radiosonde and drone-
760 dropped radiosonde based on CMA-TRAMS, *Atmos. Oceanic Sci. Lett.*,
761 18(2), <https://doi.org/10.1016/j.aosl.2024.100555>, 2025.

762 Wang, J. H. , Young, K., Hock, T., Lauritsen, D., Behringer, D., Black, M., Black, P. G., Franklin, J., Halverson,
763 J., Molinari, J., Nguyen, L., Reale, T., Smith, J., Sun, B., Wang, Q., Zhang, J. A.: A long-term, high-quality,
764 high-vertical resolution GPS dropsonde data set for hurricane and other studies, *Bull. Am. Meteorol. Soc.* ,
765 96, 961-973, <https://doi.org/10.1175/BAMS-D-13-00203.1>, 2015.

766 WMO (World Meteorological Organization): 8th WMO Workshop on the Impact of Various Observing Systems
767 on Numerical Weather Prediction and Earth System Prediction, Norrköping, Sweden,
768 <https://community.wmo.int/en/meetings/8th-wmo-impact-workshop-home>, 2024.

769 WMO (World Meteorological Organization): Guide to Meteorological Instruments and Methods of Observation,
770 Volume III - Observing Systems, WMO-No. 8, Page 464, pp., <https://library.wmo.int/idurl/4/41650>, 2025
771 edition.

772 WMO (World Meteorological Organization): Instruments and Observing Methods Report No. 143: Report of
773 WMO's 2022 Upper-Air Instruments Intercomparison Campaign, Geneva, 22
774 pp., <https://library.wmo.int/idurl/4/68808>, 2024.

775 WMO (World Meteorological Organization): The gaps in the Global Basic Observing Network (GBON), SOFF
776 Series No. 2, Page 4, pp., <https://library.wmo.int/idurl/4/57174>, 2020.

777 Xu, H. F., Guo, Q. Y., Liu, Y. Z., Lin, T. N., Ma, P. Q., and Dong, F. Z.: Key factors influencing drift success
778 rate of new-type meteorological balloons, *Journal of Applied Meteorological Science.*, 36(4), 427-440,
779 <https://doi.org/10.11898/1001-7313.20250404>, 2025. (in Chinese)

780 Yang, R. K., Wang, Y., and Liu, Q. Q.: Dynamic Performance Analysis of Sounding temperature sensor, *Sci.*
781 *Technol. Eng.*, 4 (57-60), <https://doi.org/10.3969/j.issn.1671-1815.2014.04.012>, 2014. (in Chinese)

782 Yang, J. C., Wang, Y. M., Li Q. J., Jia K. B., and Liu, P. Y.: Research on error prediction technology of
783 radiosonde temperature sensor, *Journal of Electronic Measurement and Instrumentation.*, 35(12):24-26,
784 <https://doi.org/10.13382/j.jemi.B2104288>, 2022. (in Chinese)

785 Yao, L.B., Shen, D., Sun, X., Wang, D.H., Cao, X.Z., Wang, J.C., Wang, D., Zhang, C.Y., Guo, Q.Y.: Ascent-
786 drift-descent radiosonde system: Field experiments and data quality assessment, *Atmospheric Research.*,
787 329, 108489, <https://doi.org/10.1016/j.atmosres.2025.108489>, 2026.

788 Yang, C. Y., Guo, Q.Y., Cao, X.Z., Zhang, W.: Analysis of gravity wave characteristics in the lower
789 stratosphere based on new round-trip radiosonde, *Acta Meteorologica Sinica.*, 79(1):150-167,
790 <https://doi.org/10.11676/qxxb2021.008>, 2021.(in Chinese)

791 Yang, C. Y., Cao, X.Z., Guo, Q.Y., Yuan, Y.: Feature Extraction and Analysis of Atmospheric Turbulence
792 Based on New Round-Trip Radiosonde, *Chinese Journal of Atmospheric Sciences.*, 47(6): 1967–1982,
793 <https://www.iapjournals.ac.cn/dqkx/article/exportPdf?id=bbe5bcd7-643c-4986-b364-2260622abbda>, 2023.
794 (in Chinese)

795 Zhang, X. P., Guo, Q. Y., Yang, R. K., Ma, X. L., Cao, X. Z.: Assimilation Experiment of Rainstorm in the
796 Middle and Lower Reaches of the Yangtze River Based on "ascent-drift-descent" Sounding Data, *Meteorol.*
797 *Mon.*, 47(12), 1512–1524, <https://doi.org/10.7519/j.issn.1000-0526.2021.12.007>, 2021. (in Chinese)

798 Zhang, C. Z., Huang, Y. Y., Liang, J. H., Xu, H. F.: Application Experiment of Assimilating Beidou Satellite
799 Navigation Round-Trip Sounding Data Observed in Guangdong Province Using CMA-GD Model, *Journal*
800 *of Tropical Meteorology.*, 41(1) ,16-25, <https://doi.org/10.16032/j.issn.1004-4965.2025.001>, 2025. (in
801 Chinese)

802 Zhang, X., Wang, Q. P., Ma, X. L., Zhang, X. P., Cheng, W., Xia, Y. C.: The Influence of New Round-Trip
803 Drifting Sounding Observation on the Quality of Numerical Prediction in the Middle and Lower Reaches
804 of the Yangtze River, *Chinese Journal of Atmospheric Sciences.*, 49(1): 245–256,
805 <https://doi.org/10.3878/j.issn.1006-9895.2304.22224>, 2025.(in Chinese)

806 Zhang, X. P., Sun, L., Ma, X. L., Guo, H., Gong, Z. R., Yan, X. H.: Can the Assimilation of the Ascending and
807 Descending Sections' Data from Round-Trip Drifting Soundings Improve the Forecasting of Rainstorms in
808 Eastern China?, *Atmosphere.*, 14, 1127, <https://doi.org/10.3390/atmos14071127>, 2023.

809 Zhang, X. F., Li, L. X., Yang, R. K., Guo, R., Sun, X., Luo, J. P., Chen, H. B., Liu, D. X., Tang, K. B., Peng, W.
810 W., Han, X. D., Guo, Q. Y., Li, X. X., Fei, X. K.: Comprehensive Marine Observing Experiment Based on
811 High-Altitude Large Unmanned Aerial Vehicle (South China Sea Experiment 2020 of the “Petrel
812 Project”), *Adv. Atmos. Sci.*, 38, 531–537, <https://doi.org/10.1007/s00376-020-0314-1>, 2021.

813 Zhou, X. S., Guo Q.Y., Xia Y.C., Tian, H.: Inspection of FY-3D satellite temperature data based on horizontal
814 drift round-trip sounding data, *J Appl Meteor Sci.*, 34(1): 52-64. 10.11898/1001-7313.20230105, 2023. (in
815 Chinese)

816 Zhou, X. S., Hong G., Xia Y.C., Luo H.W., Bao W.Z., Tian H.: Verification of FY-3D Satellite Humidity
817 Profiles Using Descending Phase Data of Round-Trip Drifting Sounding, *Meteor Mon.*, 50(11): 1373-1385,
818 <http://dx.doi.org/10.7519/j.issn.1000-0526.2024.063002>, 2024. (in Chinese)
819 Zhu, H. J., Li, F. Z., Kan, Z. P., He, H., Xiao, D. E., Zhang, L. Q.: Latex balloons buoyancy change analysis and
820 vertical motion trajectory simulation, *J. Rubber Ind.*, 68(8), [https://doi.org/10.12136/j.issn.1000-890-](https://doi.org/10.12136/j.issn.1000-890-x.2021.01.0017)
821 [x.2021.01.0017](https://doi.org/10.12136/j.issn.1000-890-x.2021.01.0017), 2021. (in Chinese)
822 Zhuang, Z. R., Wang, R. C., Wang, J. C., Gong, J. D.: GRAPES_Meso background error characteristics and
823 application, *J. Appl. Meteorol. Sci.*, 30(3), 316–331, <https://doi.org/10.11898/1001-7313.20190306>, 2019.
824 (in Chinese)
825